A lower affinity to cytosolic proteins reveals VDAC3 isoform-specific role in mitochondrial biology

María Queralt-Martín, María Queralt-Martín, Oscar Teijido, Nabill Munshi, Daniel Jacobs, Adam J Kuszak, Olga Protchenko, Simona Reina, Andrea Magrì, Vito de Pinto, et al.

JGP Journal of General Physiology

ARTICLE

A lower affinity to cytosolic proteins reveals VDAC3 isoform-specific role in mitochondrial biology

María Queralt-Martín[1]*, Lucie Bergdoll[2]*, Oscar Teijido[1], Nabill Munshi[2], Daniel Jacobs[1], Adam J. Kuszak[3], Olga Protchenko[4], Simona Reina[5], Andrea Magrì[5], Vito De Pinto[6], Sergey M. Bezrukov[1], Jeff Abramson[2], and Tatiana K. Rostovtseva[1]

Voltage-dependent anion channel (VDAC) is the major pathway for the transport of ions and metabolites across the mitochondrial outer membrane. Among the three known mammalian VDAC isoforms, VDAC3 is the least characterized, but unique functional roles have been proposed in cellular and animal models. Yet, a high-sequence similarity between VDAC1 and VDAC3 is indicative of a similar pore-forming structure. Here, we conclusively show that VDAC3 forms stable, highly conductive voltage-gated channels that, much like VDAC1, are weakly anion selective and facilitate metabolite exchange, but exhibit unique properties when interacting with the cytosolic proteins α-synuclein and tubulin. These two proteins are known to be potent regulators of VDAC1 and induce similar characteristic blockages (on the millisecond time scale) of VDAC3, but with 10- to 100-fold reduced on-rates and altered α-synuclein blocking times, indicative of an isoform-specific function. Through cysteine scanning mutagenesis, we found that VDAC3's cysteine residues regulate its interaction with α-synuclein, demonstrating VDAC3-unique functional properties and further highlighting a general molecular mechanism for VDAC isoform-specific regulation of mitochondrial bioenergetics.

Introduction

Permeability of mitochondrial membranes is crucial for normal metabolite exchange between mitochondria and the surrounding cytoplasm, where errors in this process result in a number of organelle pathologies (Camara et al., 2017). The voltage-dependent anion channel (VDAC), the major channel of the mitochondrial outer membrane (MOM), facilitates and controls the exchange of small ions and water-soluble respiratory substrates between these compartments (Colombini, 2004; Lemasters and Holmuhamedov, 2006; Rostovtseva and Bezrukov, 2008). There are three mammalian VDAC isoforms (VDAC1, VDAC2, and VDAC3) encoded by individual genes producing an ∼32-kD protein (Young et al., 2007) with a varied in vivo isoform distribution. In general, VDAC1 and VDAC2 show higher levels of expression (∼90%; Homblé et al., 2012; Messina et al., 2012) than VDAC3, which is far less abundant (∼10%), with an exception being the testis (Rahmani et al., 1998; Messina et al., 2012).

The mouse and human VDAC1 structures were resolved in 2008 (Bayrhuber et al., 2008; Hiller et al., 2008; Ujwal et al., 2008), revealing a transmembrane pore composed of a 19-stranded β-barrel with an N-terminal α-helix lining the pore (Fig. S1). In 2014, the high-resolution structure of zebrafish VDAC2 (Schredelseker et al., 2014) showed a very similar structure, with a root mean square deviation of 0.98 Å for all C-α atoms. Although there are no current structures of VDAC3, the high degree of sequence identity enables the construction of a reliable homology model (Fig. S1) showing a conserved 3-D structure (Amodeo et al., 2014). However, specific sequence deviations have postulated isoform-specific functional roles. One such divergence is glutamate 73, found in VDAC 1 and 2 but not in VDAC3, which is essential for pH-induced oligomerization and a possible precursor for release of apoptotic signals (Bergdoll et al., 2018). Another is the location and number of conserved cysteine residues, where VDAC1 has two cysteines (one facing

[1]Section on Molecular Transport, Eunice Kennedy Shriver National Institute of Child Health and Human Development, National Institutes of Health, Bethesda, MD; [2]Department of Physiology, David Geffen School of Medicine, University of California Los Angeles, Los Angeles, CA; [3]Laboratory of Molecular Biology, National Institute of Diabetes and Digestive and Kidney Diseases, National Institutes of Health, Bethesda, MD; [4]Liver Diseases Branch, National Institute of Diabetes and Digestive and Kidney Diseases, National Institutes of Health, Bethesda, MD; [5]Department of Biological, Geological and Environmental Sciences, University of Catania, Catania, Italy; [6]Department of Biomedical and Biotechnological Sciences, University of Catania, Catania, Italy.

*M. Queralt-Martín and L. Bergdoll contributed equally to this paper; Correspondence to Tatiana K. Rostovtseva: rostovtt@mail.nih.gov; Jeff Abramson: jabramson@mednet.ucla.edu; L. Bergdoll's present address is Laboratoire d'Ingénierie des Systèmes Macromoléculaires, UMR 7255, Centre National de la Recherche Scientifique, and Aix-Marseille Université, Marseille, France; O. Teijido's present address is Pharmanagen, Navarra Institute for Health Research, Pamplona, Navarra, Spain; A.J. Kuszak's present address is Office of Dietary Supplements, National Institutes of Health, Bethesda, MD.

the membrane and another the pore interior), while VDAC3 has six cysteines (five clustered near the intermembrane space and one in the middle of the pore; De Pinto et al., 2016; Fig. S1). In total, although structurally very similar, there are subtle sequence changes that may facilitate isoform-specific roles through yet unknown mechanisms.

Yeast complementation assays (Blachly-Dyson et al., 1993; Sampson et al., 1997; De Pinto et al., 2010; Checchetto et al., 2014) support the notion that all three VDAC isoforms share a general function of transporting ions and metabolites, but maintain isoform specific traits (Reina et al., 2010). VDAC3-knockout mice show a peculiar phenotype, male infertility, not observed with VDAC1 (Sampson et al., 2001). VDAC1- and VDAC3-deficient mice have isoform-specific alterations in mitochondrial respiration and structural aberrations observed in their isolated mitochondria that are also tissue specific (Anflous-Pharayra et al., 2011). Furthermore, isoform-specific roles in cell survival were reported, where VDAC1 selectively transferred apoptotic Ca^{2+} stimuli to mitochondria while VDAC3 had no significant influence (De Stefani et al., 2012). Additionally, VDAC3 knockdown experiments had the most pronounced effect in HepG2 cells, in particular in modulating mitochondrial membrane potential and ATP cell levels in response to microtubule-targeting drug treatment (Maldonado et al., 2013). Thus, although a common transport function may be attributed to all VDAC isoforms, there appear to be unique physiological roles that are not well understood.

When reconstituted into planar lipid membranes (PLMs), VDAC1 and 2 form highly conductive weakly anionic-selective channels that facilitate the exchange of negatively charged respiratory substrates and adenine nucleotides (Hodge and Colombini, 1997; Xu et al., 1999; Colombini, 2004; Maurya and Mahalakshmi, 2015). The transition from a high-conducting (4 nS in 1 M KCl) "open" state at low voltages to the low-conducting "closed" states (varying between 1 and 3.5 nS, in 1 M KCl) under high applied voltages is a characteristic of reconstituted VDAC1 and 2. In contrast, VDAC3 channel remains poorly characterized, largely owing to the difficulties associated with protein isolation, and the limited published results provide contradictory electrophysiological data (Xu et al., 1999; Checchetto et al., 2014; Okazaki et al., 2015; Karachitos et al., 2016; Reina et al., 2016a). While a few groups have demonstrated VDAC3 ability to form typical VDAC1-like pores (Xu et al., 1999; Okazaki et al., 2015; Karachitos et al., 2016), others reported nongating channels with small (~0.09 nS in 1 M KCl) and unstable conductance (Checchetto et al., 2014; Reina et al., 2016a). Yet, VDAC3 is commonly considered to be a regulatory protein rather than a transport channel (Ponnalagu and Singh, 2017; Han et al., 2019), contrary to the unambiguous role of VDAC1 in modulating MOM permeability (Colombini, 2004).

To generate a better understanding of VDAC3, we have purified a homogeneous sample of recombinant human VDAC3 and performed an extensive biophysical study of its channel properties. We further characterized channel properties of VDAC3 samples obtained with recombinant techniques and refolded into detergent versus samples isolated directly from the mitochondria (Colombini, 2009). In total, we compiled data from recombinant human and mouse VDAC3 expressed in *Escherichia coli* and refolded in lauryldimethylamine oxide (LDAO) and recombinant human VDAC3 expressed in yeast and isolated from mitochondria. All samples were studied under the same conditions, which is imperative because electrophysiological properties are known to be sensitive to the concentration and type of salt (NaCl vs. KCl; Rostovtseva and Bezrukov, 1998, 2015), pH (Bowen et al., 1985; Colombini, 1989; Teijido et al., 2014), and membrane lipid composition (Rostovtseva et al., 2006; Mlayeh et al., 2017; Queralt-Martín et al., 2019). We show that all VDAC3 samples used in our study exhibit basic electrophysiological properties (open channel conductance, anion selectivity, and voltage gating) similar to VDAC1, indicating that VDAC3 can concurrently facilitate metabolite exchange. Furthermore, VDAC3 demonstrates unique properties when it interacts with the cytosolic proteins α-synuclein (α-syn) and tubulin, suggesting a molecular mechanism of isoform-specific regulation of mitochondrial bioenergetics. Comparison of VDAC3 cysteine-less mutant with WT shows that reduced cysteines do not affect VDAC3 basic channel properties but alter α-syn binding kinetics. Therefore, our results provide the first indication of a unique behavior of VDAC3 as it interacts with regulatory proteins and establish VDAC3 as a potential player in mitochondrial function in health and disease.

Materials and methods

Cloning, recombinant protein production, and purification

Recombinant VDAC1 and VDAC3 WT and cysteine-less mutants expressed in Escherichia coli

Human VDAC3 and mouse VDAC1 recombinant proteins (designated as hVDAC3 and mVDAC1, respectively) were produced as described in Ujwal et al. (2008), with some differences (see Supplemental methods for details at bottom of PDF). hVDAC3 has a lower refolding yield of ~5% compared with 20% obtained for mVDAC1. Recombinant mouse VDAC3 WT (designated as mVDAC3 WT) was purified in a similar manner with modest changes in the refolding procedures (see Supplemental methods for details).

Recombinant human VDAC1 and VDAC3 WT expressed in Saccharomyces cerevisiae

Recombinant human VDAC1 and human VDAC3 (h_yVDAC1 and h_yVDAC3) WT samples were expressed in *S. cerevisiae por1Δ* BY4742 strain (*MATα his3Δ1 leu2Δ0 lys2Δ0 ura3Δ0 POR1::kanMX*; ATCC) using pYX212-hVDAC1 and pYX212-hVDAC3 plasmids (De Pinto et al., 2010). Transformants were selected and grown as previously described on synthetic complete media (Sherman, 1991) containing 2% glucose as carbon sources and lacking uracil. Mitochondria were isolated from yeast grown on synthetic complete medium containing 1.5% glycerol and 1.5% ethanol as carbon source without uracil (Lee et al., 1998). Human VDAC isoforms were purified from yeast mitochondrial membranes on a hydroxyapatite/celite (2:1) column as previously described (Blachly-Dyson et al., 1990; Palmieri and De Pinto, 1989; see Supplemental methods for details).

α-Syn and tubulin

Recombinant α-syn WT was the generous gift of Dr. Jennifer Lee (National Heart, Lung, and Blood Institute, National Institutes of Health, Bethesda, MD). α-Syn was expressed, purified, and characterized as described previously (Pfefferkorn and Lee, 2010) and stored at −80°C. Protein molecular weights were confirmed by electrospray ionization mass spectrometry (Biochemistry Core Facility, National Heart, Lung, and Blood Institute). Lyophilized porcine brain tubulin was purchased from Cytoskeleton; dissolved at 1 mg/ml in 0.1 mM PIPES buffer, pH 7.0, with 0.5 mM $MgCl_2$; aliquoted and snap frozen in liquid nitrogen; and stored at −80°C.

Thermal fluorescent protein stability assay

The melting temperatures (T_m) of both mVDAC1 and hVDAC3 were determined using the thiol-specific fluorochrome *N*-[4-(7-diethylamino-4-methyl-3-coumarinyl)phenyl]maleimide (CPM) as described previously (Alexandrov et al., 2008). In short, 40 µg of mVDAC1 (containing one exposed and one buried cysteine) or 20 µg of hVDAC3 (containing five exposed and one buried cysteine) were mixed with 16 µg of CPM in a final volume of 1 ml of buffer containing 40 mM HEPES, pH 7.0, 50 mM NaCl, and 0.1% LDAO. The reaction was transferred to a quartz cuvette and allowed to incubate on ice for 5 min. The mixture was heated in a controlled manner from 10°C to 90°C using a temperature controller. The fluorescence was recorded every 5°C on a Fluorolog spectrofluorometer at an excitation wavelength of 387 nm and an emission wavelength of 463 nm. The fluorescent signal is reduced at higher temperature due to protein aggregation; thus, the higher plateau of the unfolding profile was constrained and made equal to the maximally attainable fluorescence. The T_m was determined by fitting the data with a Boltzmann sigmoidal equation.

VDAC reconstitution and conductance measurements

PLMs were formed by apposition of two monolayers of lipid across an ∼70-µm aperture in the 15-µm-thick Teflon partition that separates two ∼1.5-ml compartments, as previously described (Rostovtseva et al., 2015). The aperture was pretreated with a 3% solution of hexadecane in pentane. PLMs were formed from lipid mixtures of dioleoyl-phosphatidylcholine (DOPC), dioleoyl-phosphatidylethanolamine (DOPE), and dioleoyl-phosphatidylglycerol (DOPG), in a ratio of 1:1:2 (wt/wt) or from soybean polar lipid extract (PLE) with 5% cholesterol (wt/wt). All lipids were purchased from Avanti Polar Lipids. Lipids were dissolved in pentane at 5 mg/ml prior monolayers formation. Typically, channel insertion was achieved 2–20 min after addition of 0.2–0.5 µl of VDAC on the Teflon partition facing the cis compartment. Short applications of large voltages up to ±200 mV helped channel insertion. For additional details of VDAC sample preparation and protocol of VDAC reconstitution into PLM, see Supplemental methods.

The membrane potential was applied using Ag/AgCl electrodes in 2 M KCl/1.5% agarose bridges assembled within standard 200-µl pipette tips. Potential is defined as positive when it is greater at the side of VDAC addition (cis side). Current recordings were performed as described previously (Rostovtseva et al., 2015) using an Axopatch 200B amplifier (Axon Instruments) in the voltage-clamp mode. Unless otherwise noted, data were filtered by a low-pass 8-pole Butterworth filter (Model 900 Frequency Active Filter, Frequency Devices) at 15 kHz, digitized with a sampling frequency of 50 kHz, and analyzed using pClamp 10.7 software (Axon Instruments).

VDAC ion selectivity was measured in 1 M (cis) versus 0.2 M KCl (trans) gradient, buffered with 5 mM HEPES at pH 7.4, as described previously (Teijido et al., 2014; see Supplemental methods). VDAC voltage-gating was measured on multichannel membranes using a previously described protocol (Colombini, 1989; Rostovtseva et al., 2006; Queralt-Martín et al., 2019; see Supplemental methods).

VDAC interactions with α-syn or tubulin were evaluated by reconstituting VDAC and monitoring a control channel current recording. Subsequently, α-syn or tubulin was added to the membrane-bathing solution to the cis or both compartments and data were acquired at different applied voltages. Records for analysis were obtained ≥20 (for α-syn) or 40 (for tubulin) min after protein addition to ensure a steady state of VDAC blocking kinetics. Data analysis was performed with Clampfit v.10.7 after a 5-kHz 8-pole Bessel digital filtering was applied. Individual events of current blockages were discriminated, and kinetic parameters were acquired by fitting a logarithmic exponential to logarithmically binned histograms (Sigworth and Sine, 1987). All lifetime histograms used 10 bins per decade. At least 300 events were collected for each analyzed current fragment. Four different logarithmic probability fits were generated using different minimization methods within the Simplex Fitting Algorithm, and the mean of the fitted time constants was used as the lifetime for the corresponding fragment. Concentrations of α-syn or tubulin in membrane bathing solutions were varied from 5 to 200 nM to achieve the number of blockage events sufficient for statistical analysis. Because normalized on-rates and blockage times do not depend on the channel blocker concentration, lifetimes were averaged for the different protein concentrations at the same applied voltage.

Electrostatic calculations using APBSmem

APBSmem (Callenberg et al., 2010) was used to carry out electrostatic calculations and ion permeation profiles on the mVDAC1 structure (3EMN) and the hVDAC3 model, obtained using the SWISS-MODEL server (https://swissmodel.expasy.org/; Bordoli et al., 2009). All calculations were performed as previously described (Marcoline et al., 2015) using a 161 × 161 × 161 grid dual level focusing. The influence of the membrane was included as a low-dielectric slab (ε = 2) with headgroup and water assigned a polar dielectric value (ε = 80). The protein dielectric constant was assigned values of ε = 5. For the ion permeation profiles, a suitable path for the ion through the middle of the pore was selected based on the N- and C-termini facing the lower bath. The ions were moved from z = 30 Å to z = −30 Å, with z = 0 in the center of the pore.

Online supplemental material

The Supplemental methods describe additional details of (a) protein purification methods, (b) ion channel reconstitution

methods, and (c) measurement of VDAC selectivity and gating. Table S1 lists conductance and selectivity of hVDAC and mVDAC samples. Figs. S1 and S2 show a comparison of structure and electrostatic potential maps of hVDAC3 and mVDAC1, respectively. Fig. S3 shows single-channel current traces of human and mouse VDAC3 and VDAC1 isolated from different sources. Fig. S4 is the extension of Fig. 3 and shows the details of the protocol of voltage application in VDAC gating experiments. Fig. S5 demonstrates uncharacteristic hVDAC3 noisy insertions. Fig. S6 shows thermal denaturation curves supplemental to Fig. 4. Figs. S7, S8, and S9 show single-channel current traces, average conductance, and ion selectivity of the cysteine-less VDAC3 and VDAC1 mutants. Fig. S10 shows free energy profiles for VDAC1 and VDAC3.

Results

VDAC3 forms stable VDAC1-like channels

Human VDAC3 (hVDAC3) was expressed in *E. coli* and refolded in LDAO detergent in a similar manner as mouse VDAC1 (mVDAC1; Ujwal et al., 2008). Purified hVDAC3 sample was reconstituted into PLM composed of a DOPC/DOPE/DOPG (1:1:2 wt/wt; DOPC/DOPE/2DOPG) lipid mixture, which mimics the high content of PC and PE lipids and preserves the negatively charged DOPG anionic lipids of the MOM (de Kroon et al., 1997). Representative single-channel current trace of hVDAC3 (Fig. 1 A) shows that the channel remains in a high-conducting or open state for a prolonged period of time under low voltages (10–30 mV). At high applied voltages (60 mV), hVDAC3 moves to low-conducting or closed states (Fig. 1 A), which is a typical behavior of reconstituted VDACs. As a comparison, a representative current trace of mVDAC1, obtained in the same experimental conditions, is shown (Fig. 1 B). Open-state conductance for hVDAC3 (3.9 ± 0.3 nS [n = 5] in 1 M KCl, pH 7.4) and mVDAC1 (4.0 ± 0.3 nS [n = 8]) shows near identical values as seen for VDACs isolated from a variety of sources (Colombini, 1989; Rostovtseva and Bezrukov, 2015).

VDAC's high conductance, or open state, features a mild preference for anions over cations, likely due to the positively charged interior of the pore (Fig. S2 A; Ujwal et al., 2008; Choudhary et al., 2010). Open-channel selectivity for hVDAC3 was measured on single or multiple channels in 1.0 M (cis)/0.2 M (trans) KCl salt gradient. Representative traces for both hVDAC3 and mVDAC1 with their corresponding I/V (current–voltage) plots are shown in Fig. 2 A. For hVDAC3, the reversal potential (the voltage corresponding to zero current) is 4.4 ± 1.4 mV (n = 5; Ψ_{rev}, indicated by green circles), which corresponds to a permeability ratio P_{Cl^-}/P_{K^+} = 1.3 ± 0.1. For mVDAC1, the reversal potential is 6.0 ± 1.0 mV (n = 13), which corresponds to a permeability ratio P_{Cl^-}/P_{K^+} = 1.4 ± 0.1 (Fig. 2 B). Although mVDAC1 has a slightly higher permeability ratio compared with hVDAC3, there is minimal significance ($P < 0.05$).

To verify these findings are species and expression system independent, the channel properties for mouse and human isoforms isolated from both inclusion bodies and from yeast mitochondria were attained. In addition to hVDAC3, mouse VDAC3 was expressed in *E. coli* and isolated from inclusion bodies (designated as mVDAC3), and human VDAC3 and VDAC1 were expressed and isolated from mitochondria of the yeast strain deficient of its endogenous VDAC1 (*Δpor1*; designated as h_yVDAC3 and h_yVDAC1). The single-channel experiments (Fig. S3 and Table S1) show that all four VDACs form ion channels with virtually undistinguishable basic channel properties when reconstituted and recorded under similar conditions.

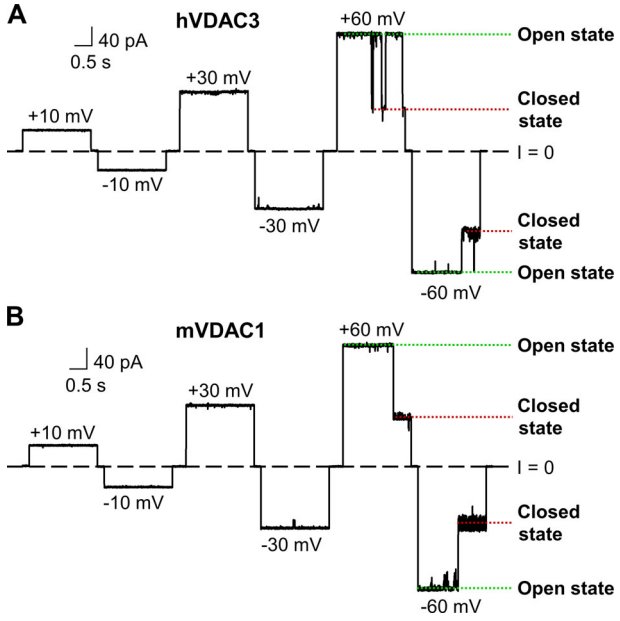

Figure 1. **hVDAC3 forms high-conducting channels with a stable open state and voltage-induced closures. (A and B)** Representative single-channel current traces obtained with reconstituted hVDAC3 (A) and mVDAC1 (B) at different applied voltages. Here, and elsewhere, dashed lines indicate zero current level and dotted lines, open and closed states of VDAC. Current records were digitally filtered at 500 Hz using a low-pass Bessel (8-pole) filter. Planar membranes were made of DOPC/DOPE/2DOPG. Membrane-bathing solutions consisted of 1 M KCl buffered with 5 mM HEPES at pH 7.4.

Voltage gating (the voltage-triggered switching between open and closed states) is a characteristic property of VDACs (Colombini, 1989; Rostovtseva et al., 2006; Teijido et al., 2012). Although single-channel recordings of VDAC3 (Figs. 1 and S3) demonstrate a gating pattern similar to other VDACs, a quantitative comparison of VDAC3 gating with VDAC1 requires a different experimental approach that incorporates PLM with multiple VDAC channels (typically 20–100). This approach allows a thorough quantification of gating properties (Schein et al., 1976; Colombini, 1989; Rostovtseva et al., 2006; Rappaport et al., 2015). Multichannel VDAC3 recordings were successfully acquired for all samples. However, mVDAC3 had the highest number of insertions and was selected for additional gating studies. In these experiments, PLM were composed of soybean PLE with 5% cholesterol, as this mixture promotes gating at lower voltages than PLM composed of DOPC/DOPE/2DOPG membranes (Queralt-Martín et al., 2019). Both mVDAC3 and mVDAC1 displayed similar current responses (Fig. S4, upper panel) to slow triangular voltage waves (Fig. S4, lower panel), showing steep slopes at low voltages (corresponding to open

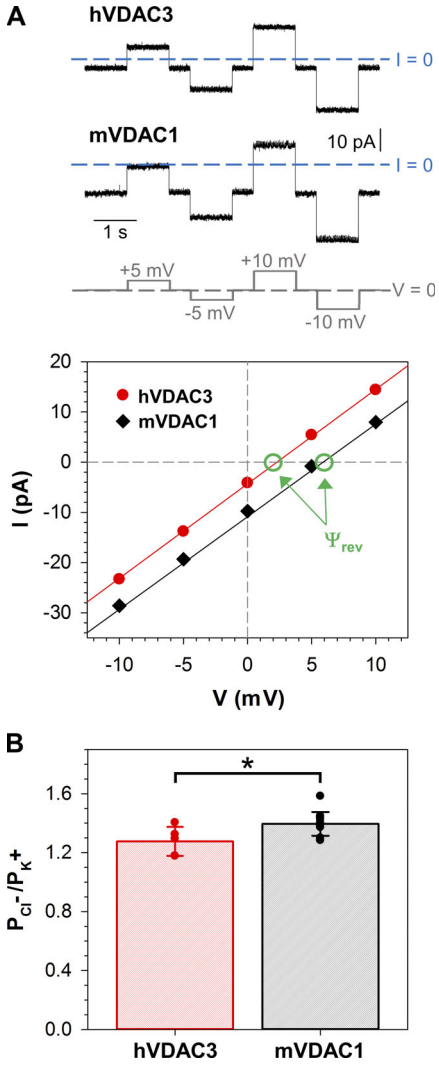

Figure 2. **hVDAC3 forms anion selective channels. (A)** Representative hVDAC3 and mVDAC1 single-channel current traces (upper panel) obtained in KCl gradient: 1 M KCl (cis) versus 0.2 M KCl (trans). The applied voltages are shown at the bottom. Corresponding I/V curves (lower panel) and linear regressions (solid lines) allow calculation of the reversal potentials (Ψ_{rev}, indicated by green circles and arrows). A positive Ψ_{rev} corresponds to an anion selectivity. **(B)** Permeability ratios, P_{Cl^-}/P_{K^+}, calculated from corresponding reversal potentials using Eq. 1 in Supplemental methods for hVDAC3 and mVDAC1. Solid circles correspond to the individual data points. Data are means of at least five independent experiments ± SD; *t* test with equal variance was used to check significance, *, P < 0.05. Planar membranes were made of DOPC/DOPE/2DOPG. KCl solutions were buffered with 5 mM HEPES at pH 7.4.

channels) and irregular shallow slopes at high voltages (corresponding to closed channels). The normalized conductance plots for mVDAC3 and mVDAC1 display the characteristic bell-shaped voltage dependence (Fig. 3 A). Under the same experimental conditions, the minimum conductance (the closed state conductance, G_{min}) is marginally higher for mVDAC3 compared with mVDAC1, indicating a lower gating for mVDAC3, yet the open probability plots overlap for the two isoforms (Fig. 3 B). The gating parameters (the effective gating charge, *n*, and the voltage at which half of the channels are open, V_0) are obtained

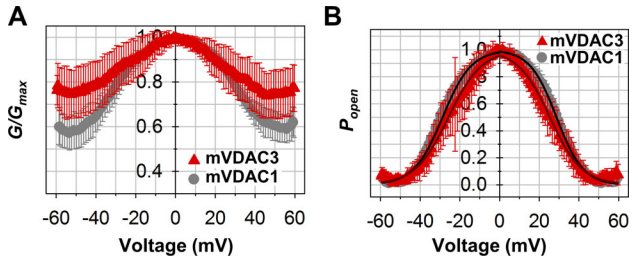

Figure 3. **Voltage-gating properties of mVDAC3 are similar to those of mVDAC1. (A and B)** Characteristic bell-shaped plots of normalized average conductance (A) and open probability, P_{open} (B), as functions of the applied voltage for mVDAC3 and mVDAC1. G/G_{max} is the normalized conductance where G_{max} is the maximum conductance at voltages closest to 0 mV. P_{open} is defined as in Eq. 2 (Supplemental methods). Solid lines in B (dark red for mVDAC3; black for mVDAC1) are the fits of P_{open} plots with the Boltzmann equation (Eq. 3 in Supplemental methods), with gating parameters *n* and V_0 presented in Table 1. Membrane solutions were buffered with 5 mM HEPES at pH 7.4. Membranes were made of PLE with 5% cholesterol (wt/wt). Data are means of 7–11 independent experiments ± SD.

from the fitting of P_{open} versus *V* plot with the Boltzmann equation (Eq. 3 in Supplemental methods; solid lines in Fig. 3 B). Table 1 shows the *n* and V_0 for mVDAC3 and mVDAC1. The gating charges are comparable for both isoforms, with a nonsignificant difference of P > 0.6 (one-way ANOVA) for negative voltages and a slightly significant difference of P < 0.05 (one-way ANOVA) at positive voltages. V_0 values obtained for mVDAC3 are consistently lower at both polarities, but this difference appears insignificant, with P > 0.2 (one-way ANOVA). Altogether, these data demonstrate that VDAC3 shares typical channel properties with VDAC1 regardless of the species or protocol of their isolation.

VDAC3 has lower protein stability than VDAC1

VDAC3 channels are more difficult to reconstitute into PLM than VDAC1 (Xu et al., 1999). Specifically, VDAC3 often formed unstable channels characterized by noisy, flickering currents that switched between different low-conducting states (*G* < 3 nS; Fig. S5). Occasionally, these channels would reach the characteristic conductance level of a fully open VDAC (Fig. S5, insets), but they were voltage independent, which is in marked contrast with the voltage-dependent closures typical for VDAC (compare Fig. S5 with Figs. 1 and S3). This same finding has been observed in previous studies (Checchetto et al., 2014; Okazaki et al., 2015), where the cysteine oxidation state was shown to contribute to protein heterogeneity during the purification procedure (Reina et al., 2016a). We relate these anomalies to the lower protein stability of VDAC3 samples solubilized in LDAO, which more easily formed aggregates during protein purification (see Materials and methods for details), requiring multiple size exclusion columns to isolate homogeneous protein (Fig. 4 A).

To quantify VDAC3's stability, a protein thermal stability assay on mVDAC1 and hVDAC3 was performed using a highly reactive thiol-specific fluorochrome (CPM; Alexandrov et al., 2008). With increasing temperatures, the protein unfolds exposing cysteine residues, which react with the CPM dye and trigger an increase in intensity. The melting temperatures for

Table 1. **Voltage gating parameters, V_0 and n, of mVDAC3 and mVDAC1**

	Positive potential		Negative potential	
	V_0(mV)	n	V_0(mV)	n
VDAC1 WT (7)	28.6 ± 1.4	3.9 ± 0.5	28.7 ± 1.9	3.6 ± 0.3
VDAC3 WT (11)	25.4 ± 3.9	3.3 ± 0.5	26.3 ± 4.7	3.4 ± 0.3

V_0, the voltage at which half of the channels are open, and n, the effective gating charge, are the fitting parameters from Fig. 3 B. Data are means ± SD, with the number of experiments indicated in parentheses.

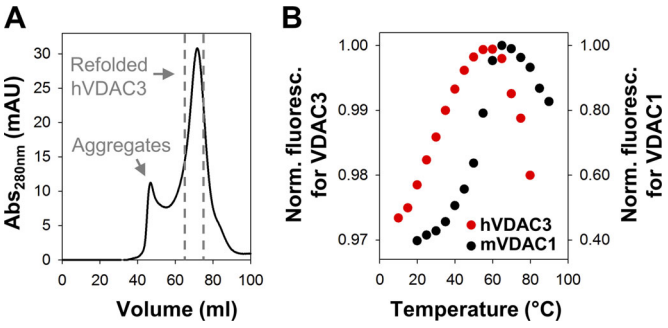

Figure 4. **VDAC3 is a less stable protein than VDAC1. (A)** Reinjection of the refolded hVDAC3 on Superdex 200 column shows a defined refolded peak separated from the first aggregate peak. Gray dashed lines indicate the fraction pooled to perform the biophysical characterization. **(B)** Melting curves of hVDAC3 (red, T_m = 29.0 ± 0.7°C) and mVDAC1 (black, T_m = 55.8 ± 0.6°C). Data are means of four to five independent experiments ± SD. For fitting procedure and error bars, see Fig. S6. Norm. fluoresc., normalized fluorescence.

hVDAC3 (T_m = 29°C) and mVDAC1 (T_m = 56°C) were recorded (Fig. 4 B), showing a dramatic shift in melting temperatures between the two isoforms (ΔT_m of 27°C). The lower T_m value for hVDAC3 is indicative of a protein with low stability when solubilized with LDAO and may explain the formation of noisy channels in the PLM due to the insertion of the unproperly folded VDAC3. In our experiments, the best insertion yield was achieved when hVDAC3 was reconstituted into PLM from hVDAC3 lipid bicelles made from 2-dimyristoyl-sn-glycero-3-phosphocholine (Ujwal and Abramson, 2012; Fig. S6).

α-Syn has a low affinity for VDAC3

Although we showed that both VDAC1 and VDAC3 can form ion channels with similar biophysical properties, a number of publications have demonstrated physiological differences between VDAC isoforms (Sampson et al., 1997, 2001; Xu et al., 1999; De Pinto et al., 2010; Reina et al., 2010; Anflous-Pharayra et al., 2011; De Stefani et al., 2012; Maldonado et al., 2013; Checchetto et al., 2014). VDAC1 has been shown to interact with the cytosolic protein α-syn, but data are lacking for other isoforms. α-Syn, a neuronal intrinsically disordered protein implicated in Parkinson's disease pathology, effectively blocks VDAC1 (Rostovtseva et al., 2015; Hoogerheide et al., 2017; Jacobs et al., 2019), where the negatively charged C-terminus of α-syn forms a functional interaction with the positively charged pore of VDAC1. We now are able to test these interactions for VDAC3.

To maximize binding of α-syn and maintain the open state of VDAC, a PLM lipid composition of DOPC/DOPE/2DOPG was used, which virtually abolishes voltage gating at applied voltages <60 mV (Queralt-Martín et al., 2019). Furthermore, the higher content of anionic DOPG in the lipid mixture increases the on-rate of α-syn with VDAC (Jacobs et al., 2019). Single-channel recordings of hVDAC3 and mVDAC1 in the presence of 10 nM of α-syn are shown in Fig. 5 A. Before α-syn addition (the initial traces in Fig. 5 A) both hVDAC3 and mVDAC1 channels remain open and maintain a stable conductance that essentially lacks transitions to the low-conductance states. Nanomolar concentrations of α-syn, added to either side of the membrane, induce rapid and well time-resolved transitions between VDAC's high-conductance open state and low-conductance blocked state (Fig. 5 A; insets at a finer time scale). For both isoforms, the conductance of α-syn–blocked state is equivalent at ∼0.4 of the open-state conductance.

The striking difference between hVDAC3 and mVDAC1 is in the frequency of α-syn–induced blockage events, where 10 nM of α-syn induces orders of magnitude fewer blockage events in hVDAC3 compared with mVDAC1 (Fig. 5 A). To quantify the blockage efficiency, we analyzed the distribution of the times when the channel is open between consequent blockages, τ_{on}, which follows an exponential distribution (Fig. 5 B) for all applied potentials. The on-rate constant, k_{on}, (the inverse of $<\tau_{on}>$ normalized over the α-syn concentration) is highly voltage dependent where it increases exponentially with the applied voltage (Rostovtseva et al., 2015; Hoogerheide et al., 2017; Jacobs et al., 2019). For hVDAC3, the k_{on} is 10- to 100-fold lower than mVDAC1 for all voltages and at both polarities (Fig. 5 C). However, the voltage dependencies of k_{on} have similar slopes for both isoforms, indicating a similar effective "binding charge" of 2.6 ± 0.3. There is a pronounced asymmetry in the on-rate values with respect to the polarity of applied voltage, with the lowest on-rates at the negative applied potentials for hVDAC3. The measurable blockage of the VDAC pore occurs when a negative potential is applied from the side of α-syn addition (Rostovtseva et al., 2015). Therefore, the negative potentials promote blockages of α-syn added to the cis side, due to the transmembrane field driving α-syn into the VDAC pore, and positive potentials promote blockages of α-syn added to the trans side (for the detailed schematic of experimental setup, see Rostovtseva and Bezrukov, 2015).

The mean time of the blockage event, τ_{off}, is also highly voltage dependent and described by exponential distributions (Fig. 5 D; Rostovtseva et al., 2015). At low applied voltages, τ_{off} increases with $|V|$, indicating a reversible capture/retraction of α-syn C-terminus by the VDAC pore. According to the established model, α-syn N-terminus is bound to the lipid membrane, thus preventing the translocation of the entire α-syn molecule through VDAC (Rostovtseva et al., 2015; Hoogerheide et al., 2017). In this regime, τ_{off} overlaps for hVDAC3 and mVDAC1 (Fig. 5 D). At higher applied voltages, τ_{off} decreases with $|V|$ (highlighted in yellow in Fig. 5 D), suggesting that α-syn translocated across the VDAC pore (Rostovtseva et al., 2015; Hoogerheide et al., 2017, 2018). V^* is the "turnover potential"

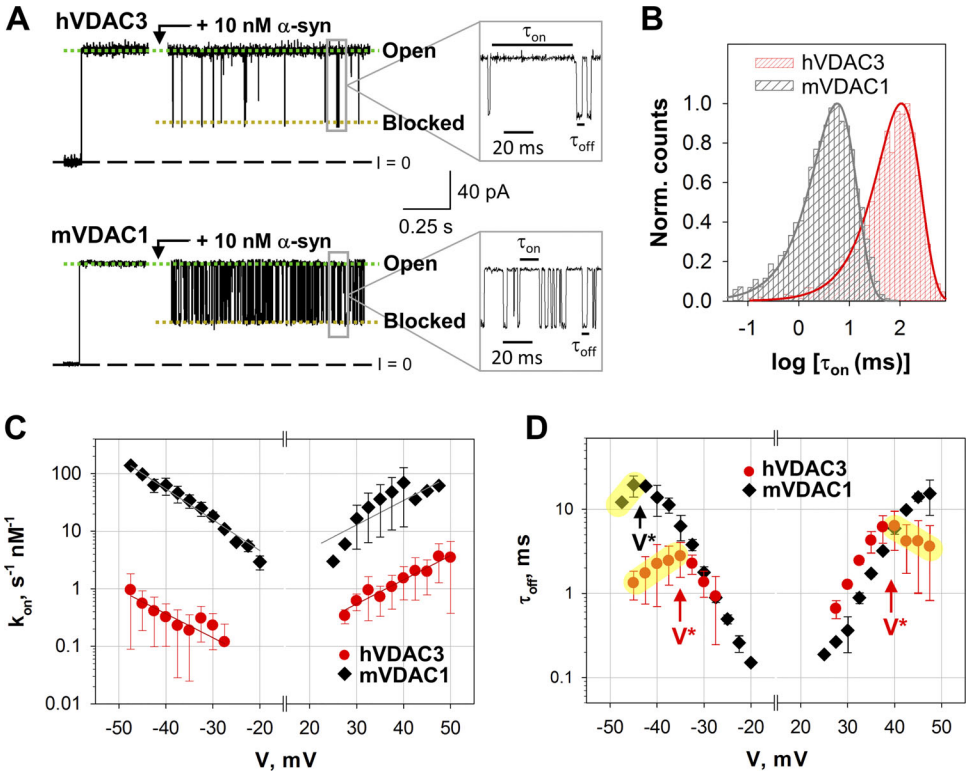

Figure 5. **α-Syn blocks hVDAC3 less efficiently than mVDAC1. (A)** Representative hVDAC3 and mVDAC1 open single-channel current traces before and after the addition of 10 nM α-syn (at +30 mV of applied voltage). Insets show fragments of current records at a finer time scale. Current records were digitally filtered at 5 kHz using a low-pass Bessel (8-pole) filter. **(B)** Log-binned distributions of the open time τ_{on} obtained with 20 nM α-syn at +30 mV for hVDAC3 and mVDAC1 and acquired from statistical analysis of the corresponding current records. Solid lines are logarithmic single-exponential fittings with characteristic times $<\tau_{on}>$ equal to 107.3 and 6.1 ms for hVDAC3 and mVDAC1, respectively. Norm., normalized. **(C)** Voltage dependences of the on-rate constant k_{on} of α-syn binding to hVDAC3 and mVDAC1. The solid lines represent a fit to Boltzmann equation $k_{on}(V) = k_0 \exp[n_b e|V|/(k_B T)]$, where V is the applied voltage, n_b is the effective binding charge of 2.6 ± 0.3, and e, k_B, and T have their usual meaning of elementary charge, Boltzmann constant, and absolute temperature, respectively. **(D)** Voltage dependences of the mean blockage time τ_{off} obtained for hVDAC3 and mVDAC1. The increase of τ_{off} with voltage amplitude corresponds to the α-syn blockage/retraction regime; the decrease of τ_{off} with voltage amplitude (highlighted in yellow) corresponds to the regime of α-syn translocation through the pore. V^* indicates the voltage separating the two regimes. Data are means of three to four experiments ± SD. Membranes were formed from mixtures of DOPC/DOPE/2DOPG, and membrane bathing solutions contained 1 M KCl buffered with 5 mM HEPES at pH 7.4.

that separates the two regimes (reversible capture/retraction vs. translocation) and clearly differs between the two isoforms. The difference in $|V^*|$ values between the two isoforms is especially pronounced at negative potentials, where α-syn starts to translocate through hVDAC3 at 10 mV lower potentials than mVDAC1 (−35 mV vs. −45 mV, respectively, indicated by vertical arrows in Fig. 5 D). The absolute values of V^* are higher at positive applied potentials than at negative for both isoforms. Taken together, these data demonstrate that α-syn interacts with VDAC3 in qualitatively similar manner to VDAC1, but the interacting kinetics differs between the two isoforms.

VDAC3 cysteines do not influence basic channel function but modulate interaction with α-syn

VDAC3 has six conserved cysteines with a heterogeneous oxidation pattern stemming from their accessibility to the oxidizing environment of mitochondrial intermembrane space (Saletti et al., 2017). These cysteine residues may be redox sensors important for channel function (De Pinto et al., 2016; Reina et al., 2016b). To address their physiological role, a cysteine-less mutant in which all six cysteine residues of hVDAC3 were replaced with alanines (hVDAC3-Δc) was generated. Additionally, a mVDAC1 cysteine-less mutant (mVDAC1-Δc) in which the two mVDAC1 cysteines were replaced with alanines was generated. For both hVDAC3-Δc and mVDAC1-Δc, the average open channel conductance had no measurable changes (Figs. S7 and S8 A), and the channels maintained their mild anionic selectivity (Fig. S8 B). At high applied voltages, hVDAC3-Δc and mVDAC1-Δc display the typical gating behavior observed in the WT sample (Fig. S7). Furthermore, the lack of cysteines did not affect the rate of proper channel insertion, with many attempts to reconstitute hVDAC3-Δc, resulting in formation of low-conducting pores with flickering current (Fig. S9), similarly to those found with WT samples (Fig. S5). This suggests that cysteines are not responsible for the low stability of hVDAC3 in PLM reconstitution. In total, hVDAC3-Δc forms typical VDAC channels.

It appears the cysteine residues do not have a significant effect on hVDAC3 stability or functionality; however, they affect hVDAC3 affinity for α-syn. α-Syn is still capable of blocking hVDAC3-Δc from both sides of the channel, similarly to WT protein (Fig. 6 A), but the on-rate of α-syn–hVDAC3-Δc interaction is ∼10 times higher than the WT hVDAC3 solely at

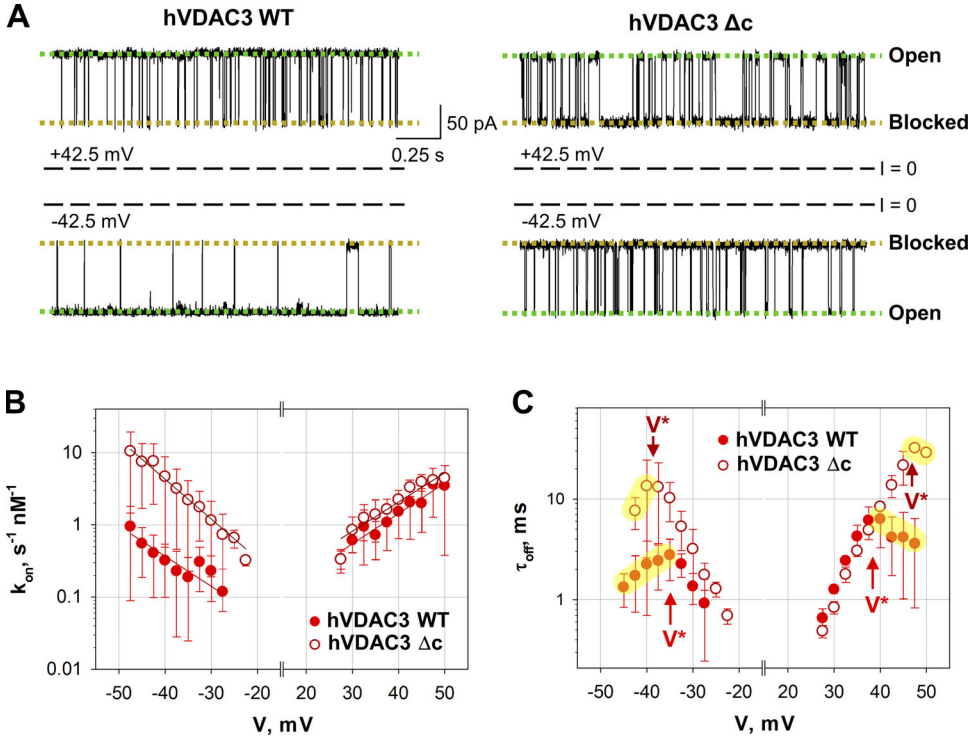

Figure 6. **Cysteines affect hVDAC3 interaction with α-syn. (A)** Representative hVDAC3 WT and hVDAC3-Δc single-channel current traces after the addition of 20 nM α-syn. The traces were recorded at ±42.5 mV of applied voltage. Current records were digitally filtered at 5 kHz using a low-pass Bessel (8-pole) filter. **(B and C)** Voltage dependence of the k_{on} (B) and mean blockage time, τ_{off} (C), of hVDAC3-Δc and hVDAC3 WT blockage by α-syn. The solid lines in B are the fits to Boltzmann equation as in Fig. 5 C, with n_b = 2.8 ± 0.4. V^* in C has the same meaning as in Fig. 5 D. Data are means of four experiments ± SD. Experimental conditions are the same as presented in Fig. 5.

negative voltage polarities (Fig. 6 B). At positive voltages, the k_{on} obtained for hVDAC3-Δc and WT are essentially the same. The slope of the k_{on} voltage dependence does not change with cysteine removal at both polarities (Fig. 6 C), indicating that cysteines do not affect the effective "binding charge" of α-syn–hVDAC3 interaction. These results suggest that the cysteines of hVDAC3 WT are responsible for the voltage asymmetry in the on-rate of α-syn-hVDAC3 interaction.

The time α-syn spends inside the channel, τ_{off}, is also affected by cysteine removal in hVDAC3 (Fig. 6 C), but to a lower extent than the time when channel is not blocked (τ_{on}). At low applied voltages, τ_{off} is essentially the same for the WT and hVDAC3-Δc at both polarities. The main difference between hVDAC3 WT and Δc is in the turnover voltage |V*|, which is 5–10 mV higher for the hVDAC3-Δc than for the WT, indicating that cysteines in hVDAC3 may facilitate α-syn translocation through the pore. Taken together, these results demonstrate that hVDAC3-Δc has no alterations in the channel's basic properties compared with WT but shows different kinetics of interaction with α-syn, which might correlate with the distinct asymmetry of cysteine distribution in VDAC3 (Fig. S1).

VDAC3 interacts with dimeric tubulin

In addition to α-syn, VDAC1 interacts with other cytosolic proteins such as dimeric tubulin, which is implicated in mitochondrial metabolism (Rostovtseva et al., 2008). The α-β-tubulin heterodimer is a 110-kD protein known as the building block of microtubules. Both tubulin and α-syn induce qualitatively similar blockages of reconstituted VDAC with nanomolar efficiency (Rostovtseva et al., 2008, 2018; Rostovtseva and Bezrukov, 2012). Based on electrophysiological measurements and molecular dynamics simulations, it was proposed that these proteins interact with VDAC in a similar multistep process. The initial association is a lipid-sensitive binding to the membrane, followed by voltage-dependent blockage of the VDAC pore, where the disordered acidic C-terminal peptide of either α-syn or tubulin is required for VDAC blockage (Rostovtseva et al., 2008, 2017; Gurnev et al., 2011; Noskov et al., 2016). According to this model, the C-terminal pore-blocking tail is tethered to an "anchor" that prevents free translocation through the pore.

Tubulin induces characteristic blockage events for both mVDAC3 and mVDAC1 (Fig. 7 A), with the residual conductance of ∼0.4 of the open state. In a similar manner as for α-syn, the efficiency of the interaction of tubulin with mVDAC3 is significantly lower than with mVDAC1. Representative current traces of single-channel experiments show that when 85 nM of tubulin is added to the cis side of the membrane, there are far fewer blockage events in mVDAC3 compared with the number of blockages induced by 45 nM in mVDAC1 (Fig. 7 A). The distribution of times between tubulin-blockage events, τ_{on}, follows a single exponential distribution for mVDAC3 and mVDAC1, as we have shown previously for VDAC isolated from mitochondria (Rostovtseva et al., 2008). The on-rate constant k_{on} of the

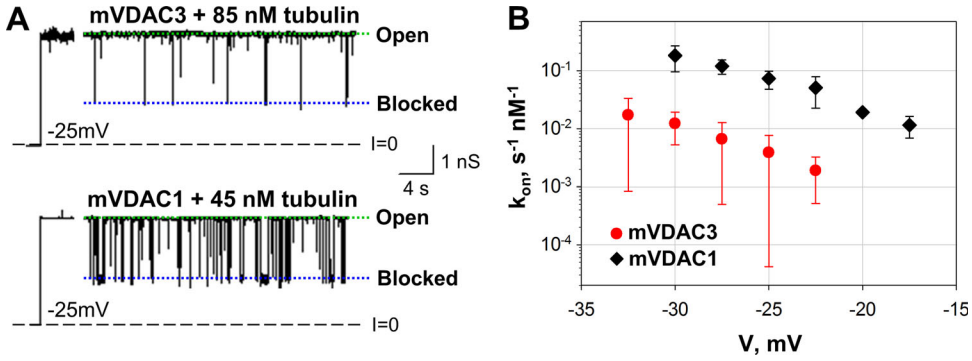

Figure 7. **Tubulin blocks mVDAC3 less efficiently than mVDAC1. (A)** Representative current traces for mVDAC3 and mVDAC1 showing time-resolved blockage events recorded at −25 mV applied voltage before and after addition of tubulin at the cis side of the membrane. Current records were digitally filtered at 500 Hz using a low-pass Bessel (8-pole) filter. **(B)** Voltage dependence of k_{on} of mVDAC3 and mVDAC1 blockage by tubulin. Data are means of 3–10 experiments ± SD. Membrane solutions were buffered with 5 mM HEPES at pH 7.4. PLM were made of PLE with 5% cholesterol (wt/wt).

interaction between tubulin and mVDAC3 is highly voltage dependent and is >10 times lower than k_{on} for mVDAC1 for all tested voltages (Fig. 7 B). Thus, these data demonstrate that similarly to α-syn, tubulin blocks VDAC3 less efficiently than VDAC1.

Discussion

VDAC is the primary transport channel in the MOM, controlling mitochondria permeability and function. The vast majority of studies involving VDAC in a wide variety of mitochondria-associated pathologies focuses exclusively on VDAC1 or VDAC2, while VDAC3 channels remain poorly characterized (Shoshan-Barmatz and Ben-Hail, 2012; Reina et al., 2016b; Camara et al., 2017; Maurya and Mahalakshmi, 2017; Shoshan-Barmatz et al., 2017). The main reason for this discrepancy stems from the difficulty in obtaining stable and homogeneous VDAC3 samples for insertions in PLM, and thus the lack of quantitative in vitro characterization. We obtained properly folded and homogeneous recombinant VDAC3 sample and successfully reconstituted into PLM, thus allowing a systematic biophysical study of VDAC3 channel properties.

All studied VDAC3 samples, hVDAC3, mVDAC3, and h_{y}-VDAC3, independent of their method of isolation and purification, were able to form stable channels with typical VDAC single-channel conductance and displaying weak anion selectivity. The anion selectivity of VDAC3 is similar to that of VDAC1 when measured under the same conditions (Fig. 2 B and Table S1), even though VDAC3 protein sequence has three additional positive charged residues compared with VDAC1 (+6 and +3, respectively; Fig. S2). However, it has previously been demonstrated that ion selectivity cannot be determined by simply counting net ion-channel protein charge; other factors such as dielectric environment and exact distribution of charged residues must be considered (Aguilella et al., 2011). We calculated ion transfer free energies for chloride and potassium ions in both hVDAC3 and mVDAC1 (Fig. S10) and found their free energy profiles to be comparable, as shown previously (Amodeo et al., 2014). These findings are consistent with the two isoforms being equally suitable conduits not only for ions but also for the negatively charged metabolites. This allows us to conclude that VDAC3, like VDAC1, most likely facilitates the passage of ATP, ADP, and other respiratory metabolites.

Voltage gating is another property of VDACs that is remarkably well conserved across different species and isoforms. The molecular mechanism of VDAC voltage gating remains poorly understood, and this is an active area of research (Mertins et al., 2012; Teijido et al., 2012; Zachariae et al., 2012; Rappaport et al., 2015; Queralt-Martín et al., 2019). Given the likely similarities in structure between VDAC1 and VDAC3 (Messina et al., 2012; Amodeo et al., 2014), a comparable gating behavior is expected for both channels. However, there have only been a few studies characterizing VDAC3 channels with little to no gating activity or with only a few successful channel insertion attempts (Xu et al., 1999; Okazaki et al., 2015; Karachitos et al., 2016). In particular, Okazaki et al. (2015) required reducing agents to observe proper VDAC3 gating. Similarly, the oxidation state of cysteines was found to be important for the insertion and activity of VDAC3 samples (Reina et al., 2016b). It must be pointed out that in these previous works, any reducing agent was avoided during purification and reconstitution steps, with the purpose of not altering the naturally occurring oxidation state of cysteines (Reina et al., 2016a; Saletti et al., 2017). In the present study, all VDAC3 samples tested showed transitions between an open state to a variety of closed states, with very similar gating characteristics to VDAC1 (Fig. 3 and Table 1). In total, purified VDAC3 solubilized in LDAO is considerably less stable than VDAC1, as demonstrated by the 27°C lower T_m than VDAC1 (Fig. 4 B) and the lower refolding yield than VDAC1. This coincides with the higher frequency of insertions of low-conductance unstable channels, which was reduced when VDAC3 was preincorporated into lipid bicelles before reconstitution. Thus, under our purification and handling conditions, VDAC3 isolated from different sources are able to form stable VDAC1-like channels.

The main difference between VDAC3 and VDAC1 isoforms stems from their interactions with α-syn, which interacts with VDAC3 10–100 times less efficiently than with VDAC1 (Fig. 5 C). VDAC3 structure is not available and we can only speculate that minor changes in channel architecture, probably subtle

differences in VDAC3 loops, could result in alterations of the lipid shell surrounding the β-barrel (Eddy et al., 2012). A modification of lipid–VDAC interface will change the energy barrier for α-syn capture by and translocation through the pore, which is reflected not only in the on-rate of the interaction, but also in the voltages at which α-syn starts to translocate (Hoogerheide et al., 2017). In accord with these notions, it was recently shown that α-syn interactions with VDAC1 are highly sensitive to the membrane lipid content (Jacobs et al., 2019). Furthermore, the structure of zebrafish VDAC2 reveals a similar structure to VDAC1, with only a subtle displacement in the loop between strands 1 and 2 (Schredelseker et al., 2014). Interestingly, electrostatic maps show significant differences in the electrostatics of the membrane-facing environment of VDAC1 and VDAC3 (Fig. S2 B), which could lead to a different lipid bilayer organization in proximity of the β-barrels of the two isoforms. Indeed, it has been shown previously that VDAC and other transmembrane proteins can distort the lipid bilayer through mechanisms such as lipid–protein interactions, hydrophobic mismatch, or lipid perturbation and sorting (O'Keeffe et al., 2000; Ellena et al., 2011; Eddy et al., 2012; Yin and Kindt, 2012; Duneau et al., 2017; Srivastava et al., 2018). In addition, a specific interaction between channel loops and PE headgroups has been proposed for plant VDAC (Mlayeh et al., 2017).

Mammalian VDAC3 features six cysteines compared with two in VDAC1, four of which are predicted to protrude toward the mitochondrial intermembrane space and have different oxidized states under physiological conditions (Saletti et al., 2017). Indeed, induction of ROS by complex III was shown to lead to cysteine oxidation of VDAC3 (Bleier et al., 2015). We did not explore here the influence of single cysteine residues on hVDAC3 basic electrophysiological properties but studied a cysteine-less hVDAC3 mutant, which shows the same basic electrophysiological properties as the WT (Figs. S7 and S8). However, the cysteine-less protein does exhibit different kinetics of α-syn–hVDAC3 interaction through an asymmetry in the on-rates at opposite voltage polarities (Fig. 6 B). This could be understood as an increase in the height of one of the entrance barriers for the α-syn molecule (Hoogerheide et al., 2017) due to the asymmetrical cysteines positioning in VDAC3 (Fig. S1). The asymmetry disappears when cysteines are removed (Fig. 6 B). Removal of cysteines also delays α-syn translocation across the pore by increasing the voltage at which translocation begins (V^*; Fig. 6 D), making voltage dependence of τ_{off} for hVDAC3-Δc similar to that of VDAC1 (Figs. 5 D and 6 D). These results suggest that cysteines modulate VDAC3 channel function in a specific way by differentially regulating its interaction with cytosolic proteins. This lends to further speculation about a possible role of the oxidation state of specific cysteine residues on α-syn-VDAC3 binding.

α-Syn interacts with VDAC3 less efficiently than VDAC1, establishing, for the first time, a clear difference between the two isoforms at the channel level. We speculate that, on a cellular level, the less efficient blockage of VDAC3 by α-syn results in VDAC3 remaining open for respiratory substrates while VDAC1 is blocked by synuclein. This may have important implications for mitochondrial bioenergetics, because VDAC blocked by α-syn is not permeable to negatively charged adenine nucleotides (Hoogerheide et al., 2017, 2018), but becomes more favorable toward Ca^{2+} transport due to the increased cationic selectivity. The differential regulation by cytosolic proteins may be a general mechanism defining the isoform specific roles of VDAC3 and VDAC1 in vivo (Messina et al., 2012), as both isoforms share very similar basic ion channel properties.

Differential affinity of VDAC isoforms for cytosolic proteins is not restricted to α-syn, but it is also seen for dimeric tubulin. Our data show that VDAC3 is blocked by tubulin 10 times less effectively than VDAC1 (Fig. 7). These results nicely support the hypothesis that VDAC3 is primarily open, when VDAC1 is closed via tubulin interaction. The results obtained with VDAC isoforms knockdown in HepG2 cells support this notion, where the level of cytosolic free tubulin was manipulated with microtubule-targeting drugs (Maldonado et al., 2013). As the tubulin-blocked state of VDAC1 is essentially impermeable to ATP (Gurnev et al., 2011), it was proposed that VDAC3, the least abundant of the VDAC isoforms, is critical for maintaining mitochondrial metabolism in these cancer cells. Future studies are needed to answer the remaining questions.

To conclude, we have unambiguously shown that VDAC3 can form typical VDAC1-like channels that conduct ions and metabolites to the same extent as VDAC1. More importantly, the dynamic interaction of VDAC3 with cytosolic proteins is a feature that distinguishes this isoform from VDAC1. This unique behavior provides, for the first time, a clue to understanding the reported differences between the functional roles of VDAC3 and VDAC1 in cell and animal models and establishes VDAC3 as potential player in mitochondrial function in health and disease.

Acknowledgments

Richard W. Aldrich served as editor.

We thank Dr. Susan Buchanan for providing resources for VDAC purification. We thank Drs. Michael Grabe and Frank Marcoline for their help with the ABPSmem program and Dr. David Hoogerheide for fruitful discussion.

M. Queralt-Martín, D. Jacobs, S.M. Bezrukov, and T.K. Rostovtseva were supported by the Intramural Research Program of the National Institutes of Health, Eunice Kennedy Shriver National Institute of Child Health and Human Development. L. Bergdoll, N. Munshi, and J. Abramson were supported by National Institutes of Health R01GM078844 and the University of California, Los Angeles Cardiovascular Theme Discovery Award. V. De Pinto acknowledges the financial support by Ministero dell'Istruzione, dell'Università e della Ricerca (PRIN 2015795S5W_005).

The authors declare no competing financial interests.

Author contributions: L. Bergdoll, N. Munshi, A.J. Kuszak, and O. Teijido produced and purified recombinant VDAC1 and VDAC3. L. Bergdoll and N. Munshi produced and purified mutated recombinant VDAC1 and VDAC3 and performed the stability assays. S. Reina, A. Magrì, and V. De Pinto produced VDAC3 plasmids. L. Bergdoll performed the electrostatic calculations and ion permeation profiles. A.J. Kuszak and O. Teijido produced and purified recombinant mouse VDAC1 and VDAC3

reconstituted into LαPC liposomes. O. Protchenko and O. Teijido produced human recombinant VDAC1 and VDAC3 in yeast. M. Queralt-Martín, O. Teijido, and D. Jacobs performed the electrophysiology experiments and data analysis. M. Queralt-Martín, T.K. Rostovtseva, S.M. Bezrukov, L. Bergdoll, and J. Abramson designed the experiments and wrote the paper.

Submitted: 30 September 2019
Accepted: 20 November 2019

References

Aguilella, V.M., M. Queralt-Martín, M. Aguilella-Arzo, and A. Alcaraz. 2011. Insights on the permeability of wide protein channels: measurement and interpretation of ion selectivity. *Integr. Biol.* 3:159–172. https://doi.org/10.1039/C0IB00048E

Alcaraz, A., E.M. Nestorovich, M.L. López, E. García-Giménez, S.M. Bezrukov, and V.M. Aguilella. 2009. Diffusion, exclusion, and specific binding in a large channel: a study of OmpF selectivity inversion. *Biophys. J.* 96: 56–66. https://doi.org/10.1016/j.bpj.2008.09.024

Alexandrov, A.I., M. Mileni, E.Y. Chien, M.A. Hanson, and R.C. Stevens. 2008. Microscale fluorescent thermal stability assay for membrane proteins. *Structure.* 16:351–359. https://doi.org/10.1016/j.str.2008.02.004

Amodeo, G.F., M.A. Scorciapino, A. Messina, V. De Pinto, and M. Ceccarelli. 2014. Charged residues distribution modulates selectivity of the open state of human isoforms of the voltage dependent anion-selective channel. *PLoS One.* 9:e103879. https://doi.org/10.1371/journal.pone.0103879

Anflous-Pharayra, K., N. Lee, D.L. Armstrong, and W.J. Craigen. 2011. VDAC3 has differing mitochondrial functions in two types of striated muscles. *Biochim. Biophys. Acta.* 1807:150–156. https://doi.org/10.1016/j.bbabio.2010.09.007

Bayrhuber, M., T. Meins, M. Habeck, S. Becker, K. Giller, S. Villinger, C. Vonrhein, C. Griesinger, M. Zweckstetter, and K. Zeth. 2008. Structure of the human voltage-dependent anion channel. *Proc. Natl. Acad. Sci. USA.* 105:15370–15375. https://doi.org/10.1073/pnas.0808115105

Bergdoll, L.A., M.T. Lerch, J.W. Patrick, K. Belardo, C. Altenbach, P. Bisignano, A. Laganowsky, M. Grabe, W.L. Hubbell, and J. Abramson. 2018. Protonation state of glutamate 73 regulates the formation of a specific dimeric association of mVDAC1. *Proc. Natl. Acad. Sci. USA.* 115:E172–E179. https://doi.org/10.1073/pnas.1715464115

Blachly-Dyson, E., S. Peng, M. Colombini, and M. Forte. 1990. Selectivity changes in site-directed mutants of the VDAC ion channel: structural implications. *Science.* 247:1233–1236. https://doi.org/10.1126/science.1690454

Blachly-Dyson, E., E.B. Zambronicz, W.H. Yu, V. Adams, E.R. McCabe, J. Adelman, M. Colombini, and M. Forte. 1993. Cloning and functional expression in yeast of two human isoforms of the outer mitochondrial membrane channel, the voltage-dependent anion channel. *J. Biol. Chem.* 268:1835–1841.

Bleier, L., I. Wittig, H. Heide, M. Steger, U. Brandt, and S. Dröse. 2015. Generator-specific targets of mitochondrial reactive oxygen species. *Free Radic. Biol. Med.* 78:1–10. https://doi.org/10.1016/j.freeradbiomed.2014.10.511

Bordoli, L., F. Kiefer, K. Arnold, P. Benkert, J. Battey, and T. Schwede. 2009. Protein structure homology modeling using SWISS-MODEL workspace. *Nat. Protoc.* 4:1–13. https://doi.org/10.1038/nprot.2008.197

Bowen, K.A., K. Tam, and M. Colombini. 1985. Evidence for titratable gating charges controlling the voltage dependence of the outer mitochondrial membrane channel, VDAC. *J. Membr. Biol.* 86:51–59. https://doi.org/10.1007/BF01871610

Callenberg, K.M., O.P. Choudhary, G.L. de Forest, D.W. Gohara, N.A. Baker, and M. Grabe. 2010. APBSmem: a graphical interface for electrostatic calculations at the membrane. *PLoS One.* 5:e12722. https://doi.org/10.1371/journal.pone.0012722

Camara, A.K.S., Y. Zhou, P.C. Wen, E. Tajkhorshid, and W.M. Kwok. 2017. Mitochondrial VDAC1: A Key Gatekeeper as Potential Therapeutic Target. *Front. Physiol.* 8:460. https://doi.org/10.3389/fphys.2017.00460

Checchetto, V., S. Reina, A. Magrì, I. Szabo, and V. De Pinto. 2014. Recombinant human voltage dependent anion selective channel isoform 3 (hVDAC3) forms pores with a very small conductance. *Cell. Physiol. Biochem.* 34:842–853. https://doi.org/10.1159/000363047

Choudhary, O.P., R. Ujwal, W. Kowallis, R. Coalson, J. Abramson, and M. Grabe. 2010. The electrostatics of VDAC: implications for selectivity and gating. *J. Mol. Biol.* 396:580–592. https://doi.org/10.1016/j.jmb.2009.12.006

Colombini, M. 1989. Voltage gating in the mitochondrial channel, VDAC. *J. Membr. Biol.* 111:103–111. https://doi.org/10.1007/BF01871775

Colombini, M. 2004. VDAC: the channel at the interface between mitochondria and the cytosol. *Mol. Cell. Biochem.* 256-257:107–115. https://doi.org/10.1023/B:MCBI.0000009862.17396.8d

Colombini, M. 2009. The published 3D structure of the VDAC channel: native or not? *Trends Biochem. Sci.* 34:382–389. https://doi.org/10.1016/j.tibs.2009.05.001

de Kroon, A.I., D. Dolis, A. Mayer, R. Lill, and B. de Kruijff. 1997. Phospholipid composition of highly purified mitochondrial outer membranes of rat liver and Neurospora crassa. Is cardiolipin present in the mitochondrial outer membrane? *Biochim. Biophys. Acta.* 1325:108–116. https://doi.org/10.1016/S0005-2736(96)00240-4

De Pinto, V., F. Guarino, A. Guarnera, A. Messina, S. Reina, F.M. Tomasello, V. Palermo, and C. Mazzoni. 2010. Characterization of human VDAC isoforms: a peculiar function for VDAC3? *Biochim. Biophys. Acta.* 1797: 1268–1275. https://doi.org/10.1016/j.bbabio.2010.01.031

De Pinto, V., S. Reina, A. Gupta, A. Messina, and R. Mahalakshmi. 2016. Role of cysteines in mammalian VDAC isoforms' function. *Biochim. Biophys. Acta.* 1857:1219–1227. https://doi.org/10.1016/j.bbabio.2016.02.020

De Stefani, D., A. Bononi, A. Romagnoli, A. Messina, V. De Pinto, P. Pinton, and R. Rizzuto. 2012. VDAC1 selectively transfers apoptotic Ca2+ signals to mitochondria. *Cell Death Differ.* 19:267–273. https://doi.org/10.1038/cdd.2011.92

Duneau, J.P., J. Khao, and J.N. Sturgis. 2017. Lipid perturbation by membrane proteins and the lipophobic effect. *Biochim Biophys Acta Biomembr.* 1859: 126–134. https://doi.org/10.1016/j.bbamem.2016.10.014

Eddy, M.T., T.C. Ong, L. Clark, O. Teijido, P.C. van der Wel, R. Garces, G. Wagner, T.K. Rostovtseva, and R.G. Griffin. 2012. Lipid dynamics and protein-lipid interactions in 2D crystals formed with the β-barrel integral membrane protein VDAC1. *J. Am. Chem. Soc.* 134:6375–6387. https://doi.org/10.1021/ja300347v

Ellena, J.F., P. Lackowicz, H. Mongomery, and D.S. Cafiso. 2011. Membrane thickness varies around the circumference of the transmembrane protein BtuB. *Biophys. J.* 100:1280–1287. https://doi.org/10.1016/j.bpj.2011.01.055

Gurnev, P.A., T.K. Rostovtseva, and S.M. Bezrukov. 2011. Tubulin-blocked state of VDAC studied by polymer and ATP partitioning. *FEBS Lett.* 585:2363–2366. https://doi.org/10.1016/j.febslet.2011.06.008

Han, J.H., J. Park, S.H. Myung, S.H. Lee, H.Y. Kim, K.S. Kim, Y.W. Seo, and T.H. Kim. 2019. Noxa mitochondrial targeting domain induces necrosis via VDAC2 and mitochondrial catastrophe. *Cell Death Dis.* 10:519. https://doi.org/10.1038/s41419-019-1753-4

Hille, B. 2001. Ion Channels of Excitable Membranes. Third. Third edition. Sinauer Associates Inc., Sunderland, MA. 814 pp.

Hiller, S., R.G. Garces, T.J. Malia, V.Y. Orekhov, M. Colombini, and G. Wagner. 2008. Solution structure of the integral human membrane protein VDAC-1 in detergent micelles. *Science.* 321:1206–1210. https://doi.org/10.1126/science.1161302

Hodge, T., and M. Colombini. 1997. Regulation of metabolite flux through voltage-gating of VDAC channels. *J. Membr. Biol.* 157:271–279. https://doi.org/10.1007/s002329900235

Homblé, F., E.M. Krammer, and M. Prévost. 2012. Plant VDAC: facts and speculations. *Biochim. Biophys. Acta.* 1818:1486–1501. https://doi.org/10.1016/j.bbamem.2011.11.028

Hoogerheide, D.P., P.A. Gurnev, T.K. Rostovtseva, and S.M. Bezrukov. 2017. Mechanism of α-synuclein translocation through a VDAC nanopore revealed by energy landscape modeling of escape time distributions. *Nanoscale.* 9:183–192. https://doi.org/10.1039/C6NR08145B

Hoogerheide, D.P., P.A. Gurnev, T.K. Rostovtseva, and S.M. Bezrukov. 2018. Real-Time Nanopore-Based Recognition of Protein Translocation Success. *Biophys. J.* 114:772–776. https://doi.org/10.1016/j.bpj.2017.12.019

Jacobs, D., D.P. Hoogerheide, A. Rovini, Z. Jiang, J.C. Lee, T.K. Rostovtseva, and S.M. Bezrukov. 2019. Probing Membrane Association of α-Synuclein Domains with VDAC Nanopore Reveals Unexpected Binding Pattern. *Sci. Rep.* 9:4580. https://doi.org/10.1038/s41598-019-40979-8

Karachitos, A., D. Grobys, M. Antoniewicz, S. Jedut, J. Jordan, and H. Kmita. 2016. Human VDAC isoforms differ in their capability to interact with

minocycline and to contribute to its cytoprotective activity. *Mitochondrion.* 28:38–48. https://doi.org/10.1016/j.mito.2016.03.004

Kuszak, A.J., D. Jacobs, P.A. Gurnev, T. Shiota, J.M. Louis, T. Lithgow, S.M. Bezrukov, T.K. Rostovtseva, and S.K. Buchanan. 2015. Evidence of Distinct Channel Conformations and Substrate Binding Affinities for the Mitochondrial Outer Membrane Protein Translocase Pore Tom40. *J. Biol. Chem.* 290:26204–26217. https://doi.org/10.1074/jbc.M115.642173

Lee, A.C., X. Xu, E. Blachly-Dyson, M. Forte, and M. Colombini. 1998. The role of yeast VDAC genes on the permeability of the mitochondrial outer membrane. *J. Membr. Biol.* 161:173–181. https://doi.org/10.1007/s002329900324

Lemasters, J.J., and E. Holmuhamedov. 2006. Voltage-dependent anion channel (VDAC) as mitochondrial governator--thinking outside the box. *Biochim. Biophys. Acta.* 1762:181–190. https://doi.org/10.1016/j.bbadis.2005.10.006

Maldonado, E.N., K.L. Sheldon, D.N. DeHart, J. Patnaik, Y. Manevich, D.M. Townsend, S.M. Bezrukov, T.K. Rostovtseva, and J.J. Lemasters. 2013. Voltage-dependent anion channels modulate mitochondrial metabolism in cancer cells: regulation by free tubulin and erastin. *J. Biol. Chem.* 288:11920–11929. https://doi.org/10.1074/jbc.M112.433847

Marcoline, F.V., N. Bethel, C.J. Guerriero, J.L. Brodsky, and M. Grabe. 2015. Membrane Protein Properties Revealed through Data-Rich Electrostatics Calculations. *Structure.* 23:1526–1537. https://doi.org/10.1016/j.str.2015.05.014

Maurya, S.R., and R. Mahalakshmi. 2015. N-helix and Cysteines Interregulate Human Mitochondrial VDAC-2 Function and Biochemistry. *J. Biol. Chem.* 290:30240–30252. https://doi.org/10.1074/jbc.M115.693978

Maurya, S.R., and R. Mahalakshmi. 2017. Mitochondrial VDAC2 and cell homeostasis: highlighting hidden structural features and unique functionalities. *Biol. Rev. Camb. Philos. Soc.* 92:1843–1858. https://doi.org/10.1111/brv.12311

Mertins, B., G. Psakis, W. Grosse, K.C. Back, A. Salisowski, P. Reiss, U. Koert, and L.O. Essen. 2012. Flexibility of the N-terminal mVDAC1 segment controls the channel's gating behavior. *PLoS One.* 7:e47938. https://doi.org/10.1371/journal.pone.0047938

Messina, A., S. Reina, F. Guarino, and V. De Pinto. 2012. VDAC isoforms in mammals. *Biochim. Biophys. Acta.* 1818:1466–1476. https://doi.org/10.1016/j.bbamem.2011.10.005

Mlayeh, L., E.M. Krammer, M. Léonetti, M. Prévost, and F. Homblé. 2017. The mitochondrial VDAC of bean seeds recruits phosphatidylethanolamine lipids for its proper functioning. *Biochim Biophys Acta Bioenerg.* 1858:786–794. https://doi.org/10.1016/j.bbabio.2017.06.005

Noskov, S.Y., T.K. Rostovtseva, A.C. Chamberlin, O. Teijido, W. Jiang, and S.M. Bezrukov. 2016. Current state of theoretical and experimental studies of the voltage-dependent anion channel (VDAC). *Biochim. Biophys. Acta.* 1858(7 Pt B, 7 Pt B):1778–1790. https://doi.org/10.1016/j.bbamem.2016.02.026

O'Keeffe, A.H., J.M. East, and A.G. Lee. 2000. Selectivity in lipid binding to the bacterial outer membrane protein OmpF. *Biophys. J.* 79:2066–2074. https://doi.org/10.1016/S0006-3495(00)76454-X

Okazaki, M., K. Kurabayashi, M. Asanuma, Y. Saito, K. Dodo, and M. Sodeoka. 2015. VDAC3 gating is activated by suppression of disulfide-bond formation between the N-terminal region and the bottom of the pore. *Biochim. Biophys. Acta.* 1848:3188–3196. https://doi.org/10.1016/j.bbamem.2015.09.017

Palmieri, F., and V. De Pinto. 1989. Purification and properties of the voltage-dependent anion channel of the outer mitochondrial membrane. *J. Bioenerg. Biomembr.* 21:417–425. https://doi.org/10.1007/BF00762514

Pfefferkorn, C.M., and J.C. Lee. 2010. Tryptophan probes at the alpha-synuclein and membrane interface. *J. Phys. Chem. B.* 114:4615–4622. https://doi.org/10.1021/jp908092e

Ponnalagu, D., and H. Singh. 2017. Anion Channels of Mitochondria. *Handb. Exp. Pharmacol.* 240:71–101. https://doi.org/10.1007/164_2016_39

Queralt-Martín, M., L. Bergdoll, D. Jacobs, S.M. Bezrukov, J. Abramson, and T.K. Rostovtseva. 2019. Assessing the role of residue E73 and lipid headgroup charge in VDAC1 voltage gating. *Biochim Biophys Acta Bioenerg.* 1860:22–29. https://doi.org/10.1016/j.bbabio.2018.11.001

Rahmani, Z., C. Maunoury, and A. Siddiqui. 1998. Isolation of a novel human voltage-dependent anion channel gene. *Eur. J. Hum. Genet.* 6:337–340. https://doi.org/10.1038/sj.ejhg.5200198

Rappaport, S.M., O. Teijido, D.P. Hoogerheide, T.K. Rostovtseva, A.M. Berezhkovskii, and S.M. Bezrukov. 2015. Conductance hysteresis in the voltage-dependent anion channel. *Eur. Biophys. J.* 44:465–472. https://doi.org/10.1007/s00249-015-1049-2

Reina, S., V. Checchetto, R. Saletti, A. Gupta, D. Chaturvedi, C. Guardiani, F. Guarino, M.A. Scorciapino, A. Magrì, S. Foti, et al. 2016a. VDAC3 as a sensor of oxidative state of the intermembrane space of mitochondria: the putative role of cysteine residue modifications. *Oncotarget.* 7:2249–2268. https://doi.org/10.18632/oncotarget.6850

Reina, S., F. Guarino, A. Magrì, and V. De Pinto. 2016b. VDAC3 As a Potential Marker of Mitochondrial Status Is Involved in Cancer and Pathology. *Front. Oncol.* 6:264. https://doi.org/10.3389/fonc.2016.00264

Reina, S., V. Palermo, A. Guarnera, F. Guarino, A. Messina, C. Mazzoni, and V. De Pinto. 2010. Swapping of the N-terminus of VDAC1 with VDAC3 restores full activity of the channel and confers anti-aging features to the cell. *FEBS Lett.* 584:2837–2844. https://doi.org/10.1016/j.febslet.2010.04.066

Rostovtseva, T.K., and S.M. Bezrukov. 1998. ATP transport through a single mitochondrial channel, VDAC, studied by current fluctuation analysis. *Biophys. J.* 74:2365–2373. https://doi.org/10.1016/S0006-3495(98)77945-7

Rostovtseva, T.K., and S.M. Bezrukov. 2008. VDAC regulation: role of cytosolic proteins and mitochondrial lipids. *J. Bioenerg. Biomembr.* 40:163–170. https://doi.org/10.1007/s10863-008-9145-y

Rostovtseva, T.K., and S.M. Bezrukov. 2012. VDAC inhibition by tubulin and its physiological implications. *Biochim. Biophys. Acta.* 1818:1526–1535. https://doi.org/10.1016/j.bbamem.2011.11.004

Rostovtseva, T.K., and S.M. Bezrukov. 2015. Function and Regulation of Mitochondrial Voltage-Dependent Anion Channel. *In* Electrophysiology of Unconventional Channels and Pores. A.H. Delcour, editor. Springer, Switzerland. 3–31. https://doi.org/10.1007/978-3-319-20149-8_1

Rostovtseva, T.K., P.A. Gurnev, D.P. Hoogerheide, A. Rovini, M. Sirajuddin, and S.M. Bezrukov. 2018. Sequence diversity of tubulin isotypes in regulation of the mitochondrial voltage-dependent anion channel. *J. Biol. Chem.* 293:10949–10962. https://doi.org/10.1074/jbc.RA117.001569

Rostovtseva, T.K., P.A. Gurnev, O. Protchenko, D.P. Hoogerheide, T.L. Yap, C.C. Philpott, J.C. Lee, and S.M. Bezrukov. 2015. α-Synuclein Shows High Affinity Interaction with Voltage-dependent Anion Channel, Suggesting Mechanisms of Mitochondrial Regulation and Toxicity in Parkinson Disease. *J. Biol. Chem.* 290:18467–18477. https://doi.org/10.1074/jbc.M115.641746

Rostovtseva, T.K., D.P. Hoogerheide, A. Rovini, and S.M. Bezrukov. 2017. Lipids in Regulation of the Mitochondrial Outer Membrane Permeability, Bioenergetics, and Metabolism. *In* Molecular Basis for Mitochondrial Signaling. T.K. Rostovtseva, editor. Springer, Switzerland. 185–216. https://doi.org/10.1007/978-3-319-55539-3_8

Rostovtseva, T.K., N. Kazemi, M. Weinrich, and S.M. Bezrukov. 2006. Voltage gating of VDAC is regulated by nonlamellar lipids of mitochondrial membranes. *J. Biol. Chem.* 281:37496–37506. https://doi.org/10.1074/jbc.M602548200

Rostovtseva, T.K., K.L. Sheldon, E. Hassanzadeh, C. Monge, V. Saks, S.M. Bezrukov, and D.L. Sackett. 2008. Tubulin binding blocks mitochondrial voltage-dependent anion channel and regulates respiration. *Proc. Natl. Acad. Sci. USA.* 105:18746–18751. https://doi.org/10.1073/pnas.0806303105

Saletti, R., S. Reina, M.G. Pittalà, R. Belfiore, V. Cunsolo, A. Messina, V. De Pinto, and S. Foti. 2017. High resolution mass spectrometry characterization of the oxidation pattern of methionine and cysteine residues in rat liver mitochondria voltage-dependent anion selective channel 3 (VDAC3). *Biochim Biophys Acta Biomembr.* 1859:301–311. https://doi.org/10.1016/j.bbamem.2016.12.003

Sampson, M.J., W.K. Decker, A.L. Beaudet, W. Ruitenbeek, D. Armstrong, M.J. Hicks, and W.J. Craigen. 2001. Immotile sperm and infertility in mice lacking mitochondrial voltage-dependent anion channel type 3. *J. Biol. Chem.* 276:39206–39212. https://doi.org/10.1074/jbc.M104724200

Sampson, M.J., R.S. Lovell, and W.J. Craigen. 1997. The murine voltage-dependent anion channel gene family. Conserved structure and function. *J. Biol. Chem.* 272:18966–18973. https://doi.org/10.1074/jbc.272.30.18966

Schein, S.J., M. Colombini, and A. Finkelstein. 1976. Reconstitution in planar lipid bilayers of a voltage-dependent anion-selective channel obtained from paramecium mitochondria. *J. Membr. Biol.* 30:99–120. https://doi.org/10.1007/BF01869662

Schredelseker, J., A. Paz, C.J. López, C. Altenbach, C.S. Leung, M.K. Drexler, J.N. Chen, W.L. Hubbell, and J. Abramson. 2014. High resolution structure and double electron-electron resonance of the zebrafish voltage-dependent anion channel 2 reveal an oligomeric population. *J. Biol. Chem.* 289:12566–12577. https://doi.org/10.1074/jbc.M113.497438

Sherman, F. 1991. Getting started with yeast. *Methods Enzymol.* 194:3–21. https://doi.org/10.1016/0076-6879(91)94004-V

Shoshan-Barmatz, V., and D. Ben-Hail. 2012. VDAC, a multi-functional mitochondrial protein as a pharmacological target. *Mitochondrion.* 12: 24–34. https://doi.org/10.1016/j.mito.2011.04.001

Shoshan-Barmatz, V., Y. Krelin, A. Shteinfer-Kuzmine, and T. Arif. 2017. Voltage-Dependent Anion Channel 1 As an Emerging Drug Target for Novel Anti-Cancer Therapeutics. *Front. Oncol.* 7:154. https://doi.org/10.3389/fonc.2017.00154

Sigworth, F.J., and S.M. Sine. 1987. Data transformations for improved display and fitting of single-channel dwell time histograms. *Biophys. J.* 52: 1047–1054. https://doi.org/10.1016/S0006-3495(87)83298-8

Srivastava, S.R., P. Zadafiya, and R. Mahalakshmi. 2018. Hydrophobic Mismatch Modulates Stability and Plasticity of Human Mitochondrial VDAC2. *Biophys. J.* 115:2386–2394. https://doi.org/10.1016/j.bpj.2018.11.001

Teijido, O., S.M. Rappaport, A. Chamberlin, S.Y. Noskov, V.M. Aguilella, T.K. Rostovtseva, and S.M. Bezrukov. 2014. Acidification asymmetrically affects voltage-dependent anion channel implicating the involvement of salt bridges. *J. Biol. Chem.* 289:23670–23682. https://doi.org/10.1074/jbc.M114.576314

Teijido, O., R. Ujwal, C.O. Hillerdal, L. Kullman, T.K. Rostovtseva, and J. Abramson. 2012. Affixing N-terminal α-helix to the wall of the voltage-dependent anion channel does not prevent its voltage gating. *J. Biol. Chem.* 287:11437–11445. https://doi.org/10.1074/jbc.M111.314229

Ujwal, R., and J. Abramson. 2012. High-throughput crystallization of membrane proteins using the lipidic bicelle method. *J. Vis. Exp.* 59:e3383.

Ujwal, R., D. Cascio, J.P. Colletier, S. Faham, J. Zhang, L. Toro, P. Ping, and J. Abramson. 2008. The crystal structure of mouse VDAC1 at 2.3 A resolution reveals mechanistic insights into metabolite gating. *Proc. Natl. Acad. Sci. USA.* 105:17742–17747. https://doi.org/10.1073/pnas.0809634105

Xu, X., W. Decker, M.J. Sampson, W.J. Craigen, and M. Colombini. 1999. Mouse VDAC isoforms expressed in yeast: channel properties and their roles in mitochondrial outer membrane permeability. *J. Membr. Biol.* 170:89–102. https://doi.org/10.1007/s002329900540

Yin, F., and J.T. Kindt. 2012. Hydrophobic mismatch and lipid sorting near OmpA in mixed bilayers: atomistic and coarse-grained simulations. *Biophys. J.* 102:2279–2287. https://doi.org/10.1016/j.bpj.2012.04.005

Young, M.J., D.C. Bay, G. Hausner, and D.A. Court. 2007. The evolutionary history of mitochondrial porins. *BMC Evol. Biol.* 7:31. https://doi.org/10.1186/1471-2148-7-31

Zachariae, U., R. Schneider, R. Briones, Z. Gattin, J.P. Demers, K. Giller, E. Maier, M. Zweckstetter, C. Griesinger, S. Becker, et al. 2012. β-Barrel mobility underlies closure of the voltage-dependent anion channel. *Structure.* 20:1540–1549. https://doi.org/10.1016/j.str.2012.06.015

Supplemental material

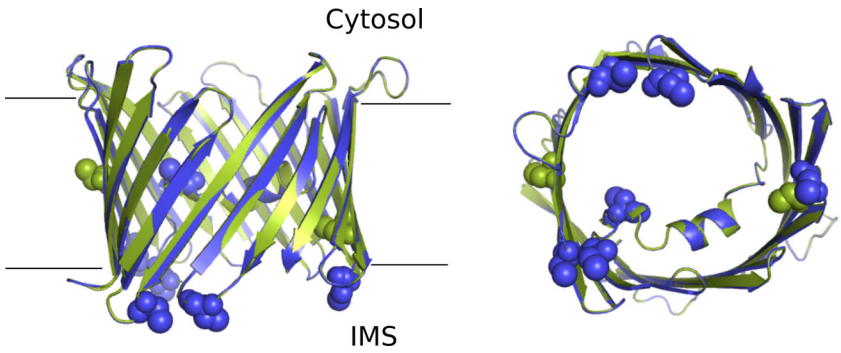

Figure S1. **Schematic representation of mVDAC1 and a model of hVDAC3.** Schematic representation of mVDAC1 (green, PDB accession no. 3EMN) and a model of hVDAC3 (blue), from the membrane plane (left), and from the intermembrane space (IMS, right). The cysteine residues are presented as spheres.

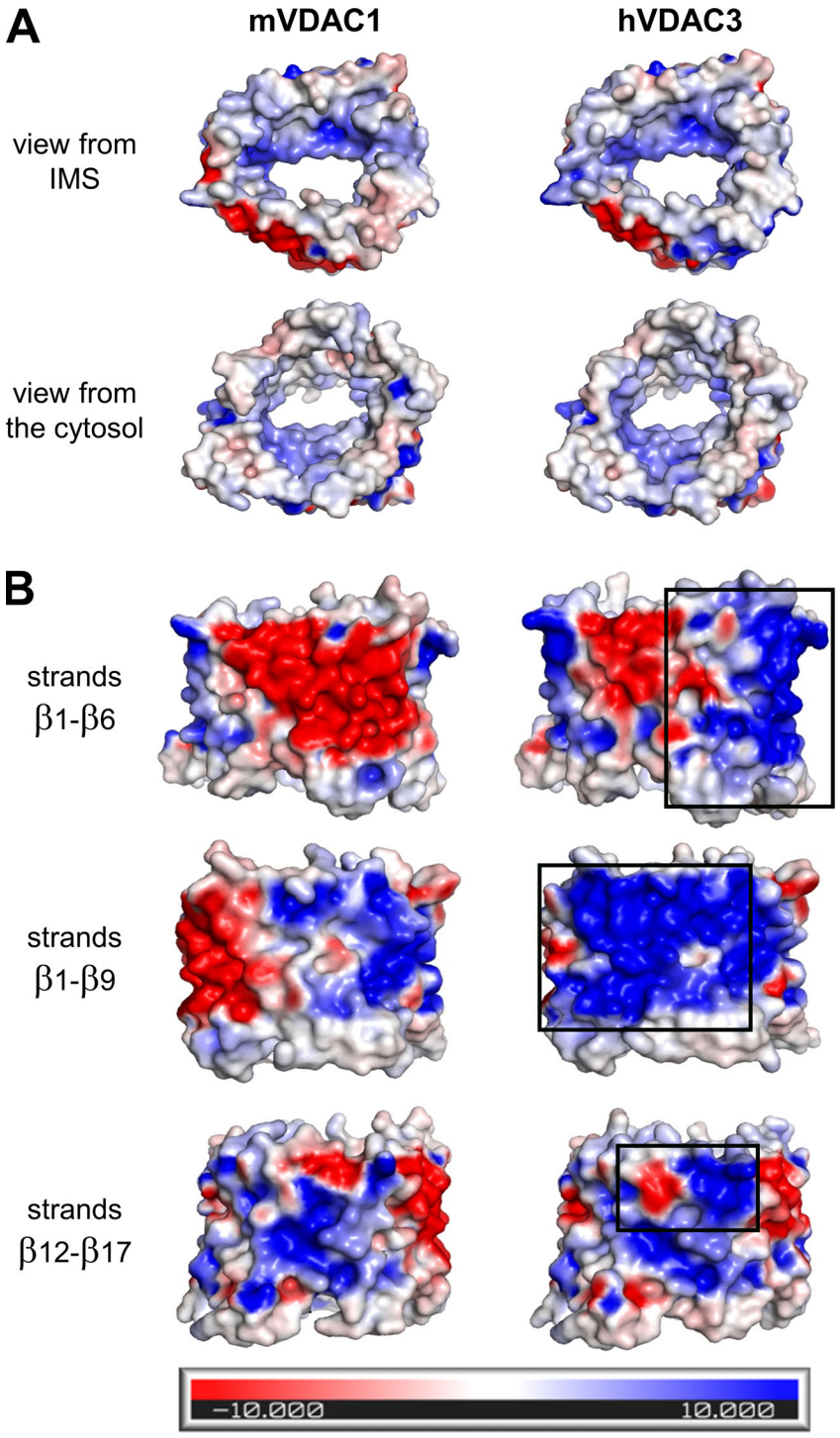

Figure S2. **Side-by-side comparison of electrostatic potential maps of mVDAC1 (left) and hVDAC3 (right). (A)** View of the pore interior. **(B)** View of the membrane domain. Black rectangles correspond to the area of most changes. These maps were generated using the APBSmem program, which takes into account the low dielectric constant of the hydrophobic membrane. Blue represents a positive potential, and red, a negative potential.

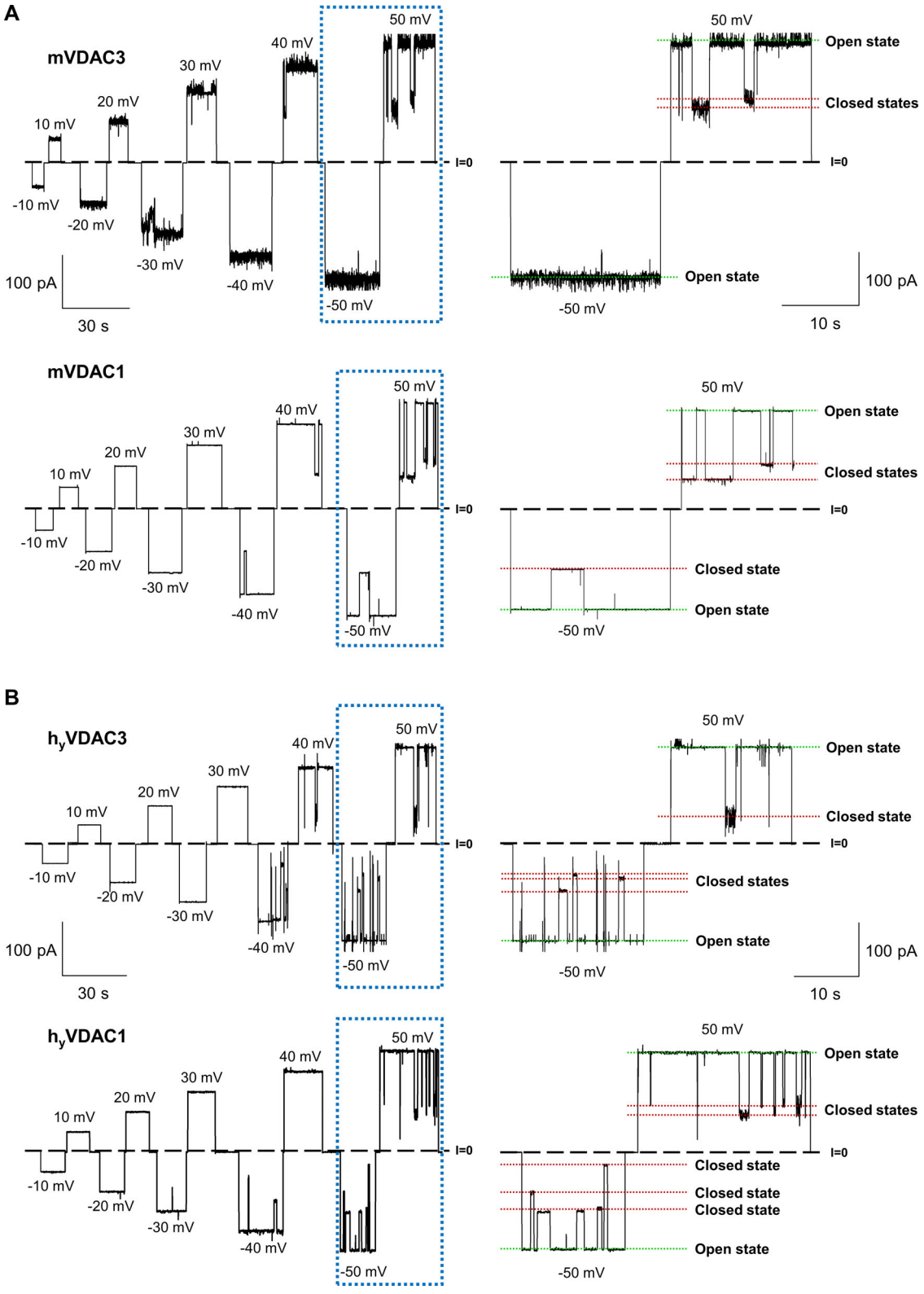

Figure S3. **Recombinant mouse VDAC3 and VDAC1 isolated from *E. coli* inclusion bodies (mVDAC3 and mVDAC1) and human VDAC3 and VDAC1 isolated from yeast mitochondria (h_yVDAC3 and h_yVDAC1) form typical VDAC channels. (A and B)** Representative single-channel current traces obtained with reconstituted mVDAC3 and mVDAC1 expressed in *E. coli* and refolded from inclusion bodies (A), and h_yVDAC3 and h_yVDAC1 expressed in yeast and isolated from mitochondria (B), at different applied voltages. Framed traces are displayed in fine time scale on the right. Dashed line indicates zero current level and dotted lines indicate VDAC's open and closed states. Current records were digitally filtered at 100 Hz using a low-pass Bessel (8-pole) filter. Membrane-bathing solutions consisted of 1 M KCl buffered with 5 mM HEPES at pH 7.4. Planar membranes were formed from soybean PLE with 5% cholesterol (wt/wt).

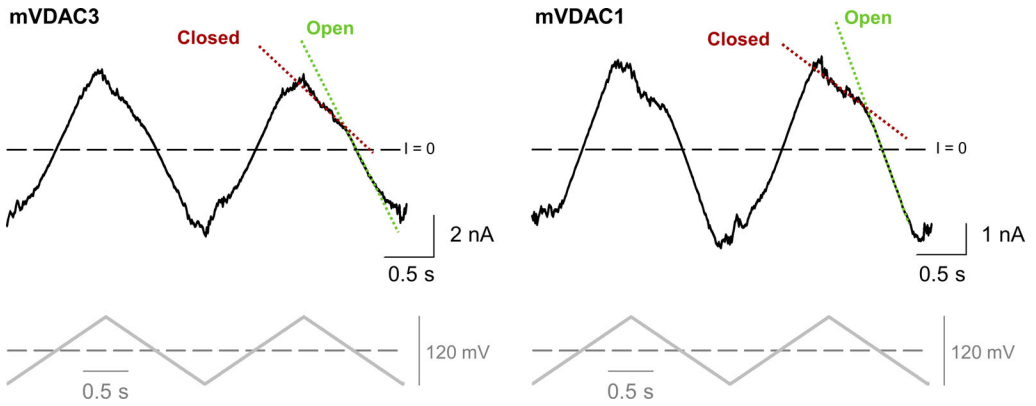

Figure S4. **Voltage-gating properties of mVDAC3 are similar to those of mVDAC1.** Representative ion current traces (upper panel), obtained on membranes with multiple reconstituted mVDAC3 and mVDAC1, in response to a triangular wave voltage (5 mHz, ± 60 mV, lower panels). Steep slopes at low potentials correspond to the open states (green dotted lines), whereas the lower slopes at higher potentials correspond to the closed states (red dotted lines). Dashed lines indicate zero current. Membrane solutions were buffered with 5 mM HEPES at pH 7.4. Membranes were made of PLE with 5% cholesterol (wt/wt).

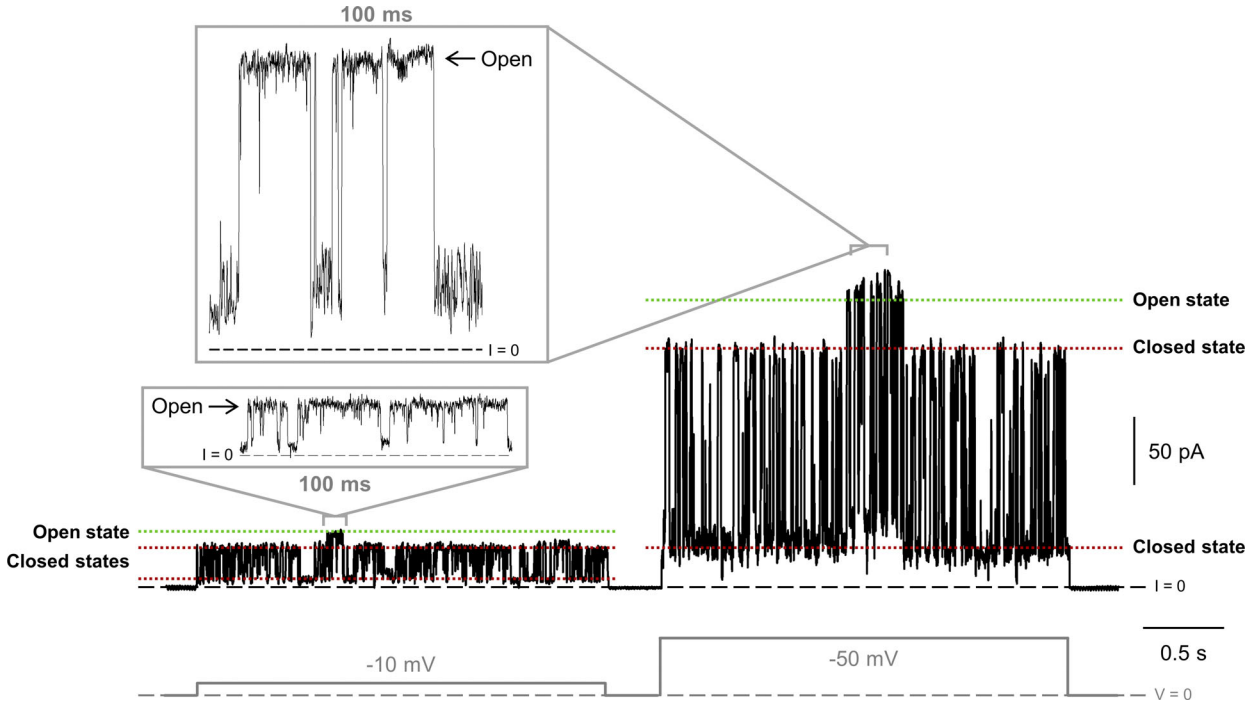

Figure S5. **hVDAC3 frequently forms uncharacteristically low-conducting pores with flickering current.** Representative current traces obtained with hVDAC3 at –10 and –50 mV applied voltages (gray, lower panel). The ion current flickers between different low-conducting levels and occasionally reaches the level corresponding to the VDAC fully open state of 4 nS. Current records were digitally filtered at 500 Hz using a low-pass Bessel (8-pole) filter. Membranes were formed from DOPC/DOPE/2DOPG. Membrane-bathing solutions consisted of 1 M KCl buffered with 5 mM HEPES at pH 7.4.

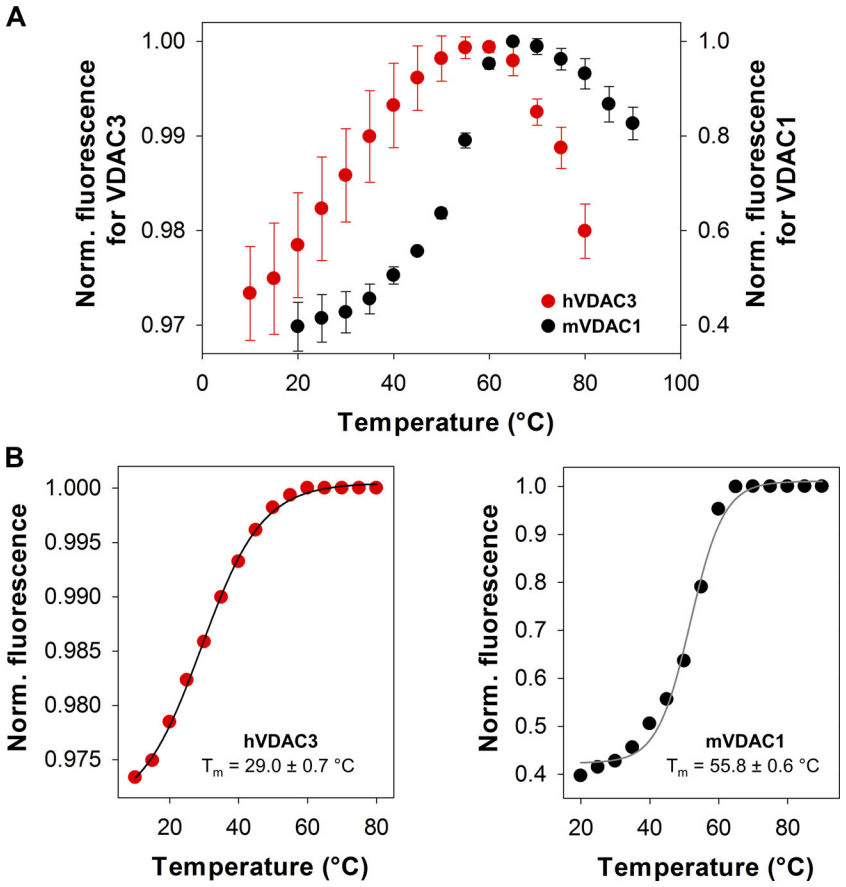

Figure S6. **VDAC3 solubilized in LDAO is a more unstable protein than VDAC1. (A)** Thermal denaturation curves of hVDAC3 (red) and mVDAC1 (black). The data are the same as in Fig. 4 B but with error bars (SD) resulting from three replicates. Norm., normalized. **(B)** For fitting purposes, the top plateau of the unfolding profile in A was constrained and made equal to the maximally attainable fluorescence. Solid lines represent the fitting for hVDAC3 (left) and mVDAC1 (right) denaturation curves using a Boltzmann sigmoidal equation.

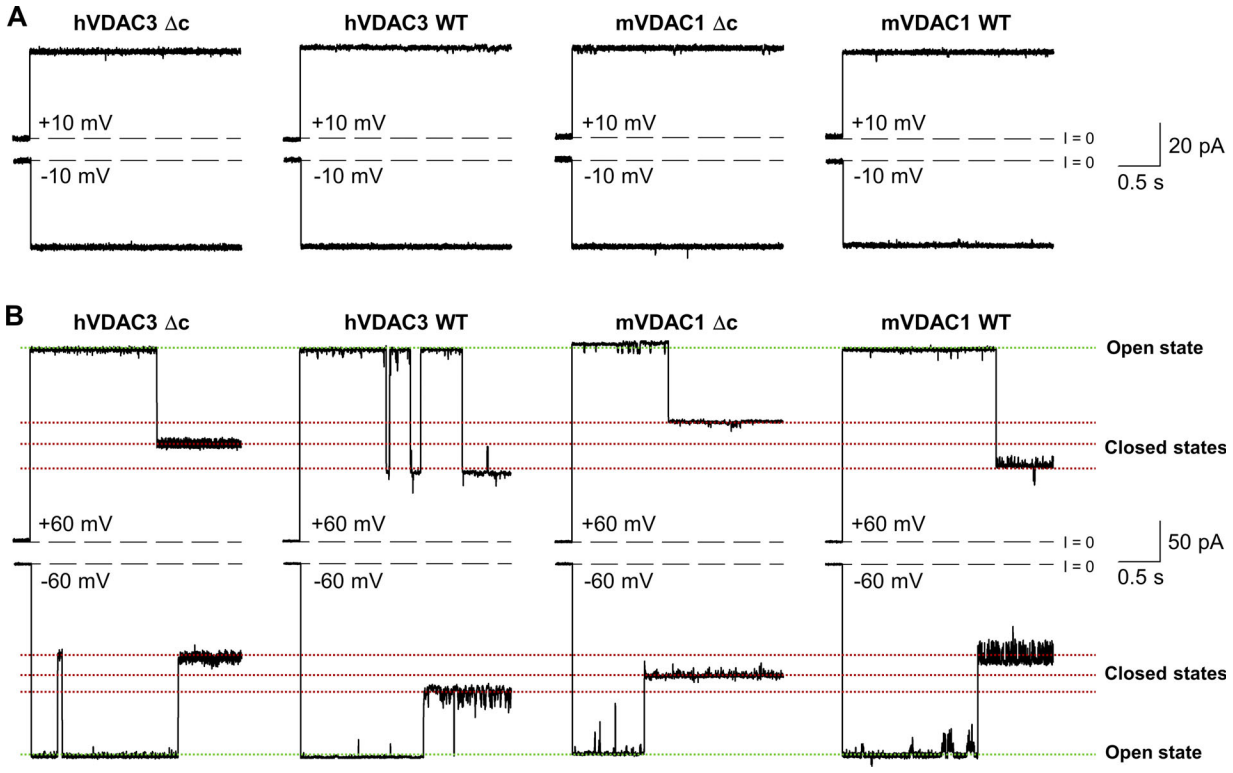

Figure S7. **Cysteine-less hVDAC3-Δc and mVDAC1-Δc form high-conducting channels with a stable open state and voltage-induced closures typical for VDAC1 and VDAC3 WT channels. (A and B)** Representative single-channel current traces obtained with reconstituted hVDAC3 WT, hVDAC3-Δc, and mVDAC1 WT, mVDAC1-Δc at low (±10 mV, A) or high (±60 mV, B) applied voltages. Current records were digitally filtered at 500 Hz using a low-pass 8-pole Bessel filter. Membranes were formed from DOPC/DOPE/2DOPG. Membrane-bathing solutions consisted of 1 M KCl buffered with 5 mM HEPES at pH 7.4.

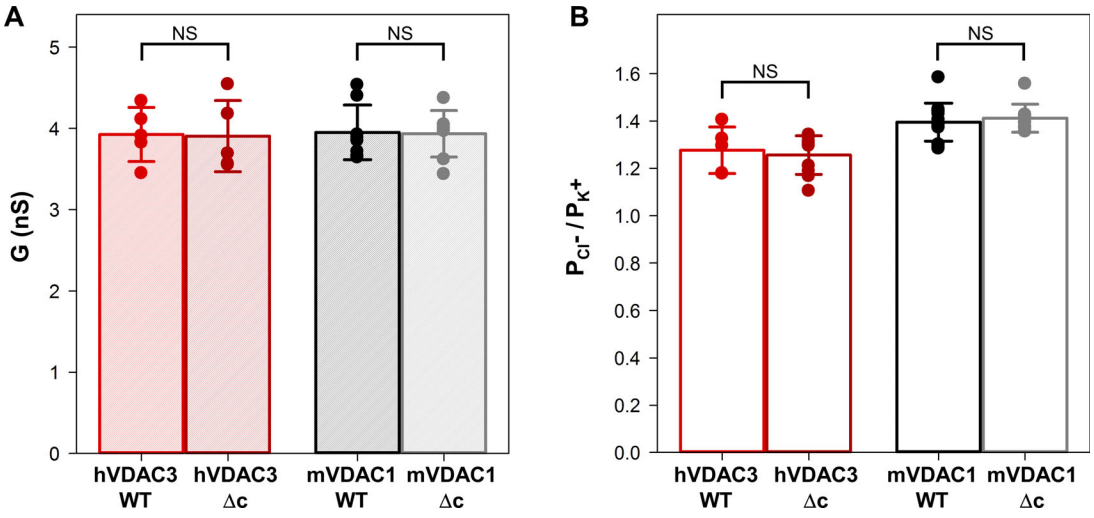

Figure S8. **hVDAC3 and mVDAC1 cysteine-less (Δc) mutants have open channel conductance and ion selectivity similar to WT. (A and B)** Bar graphs showing the open channel conductance (A) and ion selectivity (B) of hVDAC3 and mVDAC1, WT, and Δc. In A, salt solution was 1 M KCl. In B, the selectivity is presented as the permeability ratio of anions over cations in 1 M/0.2 M KCl gradient. Solid circles correspond to the data points of individual experiments. Data are means of at least five independent experiments ± SD. Student's *t* test with equal variance was used to check significance; NS, P > 0.5. The other experimental conditions are as in Fig. S7.

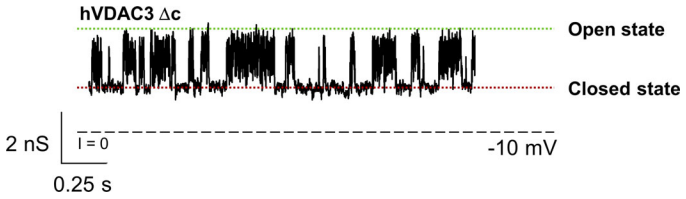

Figure S9. **VDAC3-Δc recurrently forms low-conducting pores with flickering current.** Representative single-channel current trace obtained with reconstituted VDAC3-Δc at −10 mV applied voltage. Dashed line indicates zero current level. Current records were digitally filtered at 500 Hz using a low-pass Bessel (8-pole) filter. Membranes were formed from DOPC/DOPE/2DOPG. Membrane-bathing solutions consisted of 1 M KCl buffered with 5 mM HEPES at pH 7.4.

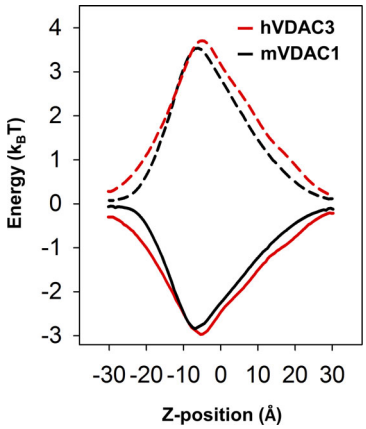

Figure S10. **VDAC3 has a free energy profile similar to that of VDAC1.** Ion transfer free energies for a chloride anion (solid lines) and a potassium cation (dashed lines) calculated for hVDAC3 (red) and mVDAC1 (black; see Materials and methods).

Provided online is one supplemental table. Table S1 shows that VDAC forms ion channels with similar open-channel conductance and ion selectivity independent on isoform, species, and isolation protocol.

Supplemental methods

Mouse recombinant VDAC1 (mVDAC1) WT and cysteine-less proteins were cloned into pQE9 plasmid in M15 cells. Human recombinant VDAC3 (hVDAC3) WT and cysteine-less proteins were cloned in the pET21a vector and expressed in BL21 (DE3) competent cells (New England BioLabs). Mouse recombinant VDAC3 (mVDAC3) was inserted in pET28a vector and expressed in T7 Express Competent *E. coli* (New England BioLabs). All cells were grown in Luria broth media with agitation at 37°C. Protein production was induced with 0.5 mM isopropyl-1-thio-β-D-galactopyranoside at an OD of 0.6–0.8 for 4 h. Cells were harvested by centrifugation and resuspended in 50 mM Tris HCl (pH 8.0), 2 mM EDTA, and 20% sucrose. The cell slurry was lysed by consecutive incubation with 12.5 µg/ml lysozyme and 0.6% Triton X-100 followed by sonication. Inclusion bodies were isolated through centrifugation at 12,000 *g* for 15 min, and solubilized in 20 mM Tris HCl (pH 8.0), 300 mM NaCl, and 6 M guanidinium hydrochloride. Denatured proteins were purified in 6 M guanidinium using a Talon metal affinity column (Takarabio). mVDAC1 proteins were refolded by three-step dialysis at 4°C: (1) 20 mM Tris HCl, pH 8.0, 300 mM NaCl, 1 mM DTT, and 3 M guanidinium hydrochloride; (2) 20 mM Tris HCl, pH 8.0, 150 mM NaCl, 1 mM DTT, and 0.1% LDAO; and (3) 20 mM Tris HCl, pH 8.0, 150 mM NaCl, 1 mM DTT, and 0.1% LDAO. The protein concentration for refolding was 5 mg/ml, and 2% LDAO was added to the protein solution before the second dialysis step. The same protocol was applied to hVDAC3 proteins, except that refolding was performed at 1 mg/ml to reduce protein aggregation during refolding. Refolded proteins were concentrated using Amicon 50 kDa. To remove precipitated protein, the concentrated sample was ultracentrifuged (355,000 *g*, 30 min) and injected on a Superdex 200 size-exclusion chromatography (SEC) column in 150 mM NaCl, 0.1% LDAO, 20 mM Tris HCl, pH 8.0, and 1 mM DTT. The refolded hVDAC3 protein peak was then reinjected on the SEC column to further separate aggregates and isolate homogeneous folded sample (Fig. 4 A).

mVDAC3 WT was purified in a similar manner with modest changes in the refolding procedures. Protein refolding was accomplished by dialyzing twice against a buffer containing 50 mM Tris, pH 7.2, 120 mM NaCl, 5 mM tris(2-carboxyethyl)phosphine (TCEP), and 1.5% LDAO detergent with continuous stirring. Refolded protein was then subjected to two rounds of 10-fold dialysis against 50 mM Tris-HCl, pH 7.2, 150 mM NaCl, 1 mM TCEP, and 0.1% LDAO. Refolded protein was run on a Ni-NTA column (GE

Healthcare) in 30 mM Tris, pH 7.2, 200 mM NaCl, 0.5 mM TCEP, and 0.1% LDAO, and protein was eluted with 30 mM Tris, pH 7.2, 200 mM NaCl, 0.05 mM TCEP, 0.075% LDAO, and 300 mM imidazole and concentrated in Amicon Centriprep YM-30 kDa (Millipore) centrifugal filter concentrators for final volumes >5 ml and Amicon Ultra Centrifugal (Millipore) units for final volumes <5 ml to a final concentration of 1 mg/ml. Protein aggregates were separated from the final pool of refolded protein by SEC with a HiPrep 16/60 Sephacryl S-300 HR preparative columns (GE Healthcare) run in 50 mM Tris, pH 7.4, 200 mM NaCl, 0.5 mM TCEP, and 0.1% LDAO.

h_yVDAC3 and h_yVDAC1 were purified from yeast mitochondrial membranes on a hydroxyapatite/celite (2:1) column as previously described (Palmieri and De Pinto, 1989; Blachly-Dyson et al., 1990). Briefly, mitochondria were centrifuged at 14,000 *g* for 20 min at 4°C. Pellets were homogenized (1:1) with mitochondrial buffer containing 10 mM Tris HCl, pH 7.0, 50 mM KCl, 1 mM EDTA, 15% DMSO, and 2.5% Triton X-100 and incubated at 4°C for 45 min. Homogenate was again centrifuged at 14,000 *g* for 20 min at 4°C, and supernatants containing mitochondrial proteins were loaded to a hydroxyapatite/celite (2:1) column followed by elution with mitochondrial buffer in 100-µl fractions.

Prior addition to the PLM chamber, mVDAC1 WT, mVDAC1-Δc, and hVDAC3-ΔC were diluted 10–100× in buffer containing 100 mM Tris, 50 mM KCl, 1 mM EDTA, 15% (vol/vol) DMSO, and 2.5% (vol/vol) Triton X-100, pH 7.35, to a final concentration of 30–300 ng/µl. hVDAC3 WT was either diluted in the same buffer to a final concentration of 15–115 ng/µl or reconstituted in 6–30% 2-dimyristoyl-sn-glycero-3-phosphocholine:CHAPSO bicelles following the protocol described in Ujwal and Abramson (2012) to a final concentration of 200–360 ng/µl. mVDAC3 WT was reconstituted into L-α-PC liposomes (Avanti Polar Lipids) as previously described (Kuszak et al., 2015) with minor modifications. Briefly, L-α-PC was solubilized in chloroform at 10 mg/ml, lyophilized under N_2 gas, and resuspended at 10 mg/ml in 50 mM Tris, pH 7.4, 50 mM NaCl, and 1 mM EDTA followed by vortexing and two cycles of bath sonication. Next, LDAO (at a final concentration of 2.0%) and purified mVDAC3 (at a final weight ratio of 100:1 lipid/protein) were added to the premade liposomes. Proteoliposomes were incubated in BioBeads SM-2, at a weight ratio of 1:30 lipid/BioBeads. Beads were removed by low-speed centrifugation. Finally, supernatant containing mVDAC3 proteoliposomes was centrifuged at 45,000 *g* for 1 h at 20°C, and the pellet containing mVDAC3 proteoliposomes was gently resuspended in 20 mM Tris, pH 7.4, 150 mM NaCl, and 1 mM EDTA at one-fifth the volume of the initial reconstitution.

VDAC channels were considered properly inserted into the planar membrane only when having a steady conductance of ∼4 nS in 1 M KCl or 2.0 nS in 1.0/0.2 M KCl gradient, a characteristic value for open-state VDAC (Teijido et al., 2014). Noisy, unstable, low-conducting or non-gated channels were recorded and analyzed but not used for further characterization of VDAC3 gating or VDAC3 interaction with α-syn and tubulin, due to the lack of stability of these insertions. The rate of successful channel insertions for all detergent-solubilized VDAC3 samples was particularly low (<20% of 150 reconstitution attempts) and substantially increased when reconstituted from lipid bicelles rather than detergent micelles (∼40% of 40 reconstitution attempts). There was no noticeable improvement of proper channel reconstitution rate when VDAC3 samples were preincubated with 10 mM DTT either by overnight incubation of the refolded VDAC3 protein at −20°C before channel reconstitution into PLM or by direct addition of the protein into the membrane bathing solution. The basic properties of VDAC3 channels, such as conductance, selectivity, and gating, did not depend on the protocol of their reconstitution into PLM.

VDAC ion selectivity was inferred from the potential corresponding to the intersection of the I/V plot, which proved to be linear in the range of ±30 mV, with the zero-current level, the reversal potential. The reversal potential was measured on one or several channels in 1 M (cis) versus 0.2 M KCl (trans) gradient, buffered with 5 mM HEPES at pH 7.4. The measured reversal potential was corrected by the liquid junction potential calculated from Henderson's equation (Alcaraz et al., 2009) to obtain the final reversal potential Ψ_{rev}, which was used to calculate permeability ratios between K^+ and Cl^-, P_{Cl^-}/P_{K^+}, according to the Goldman–Hodgkin–Katz equation (Hille, 2001):

$$P_{Cl^-} \Big/ P_{K^+} = \left(1 - \frac{\psi_{rev}}{\frac{k_B T}{e} \cdot \ln \frac{a_{trans}}{a_{cis}}}\right) \cdot \left(1 + \frac{\psi_{rev}}{\frac{k_B T}{e} \cdot \ln \frac{a_{trans}}{a_{cis}}}\right)^{-1}, \quad (1)$$

where k_B, T, and e have their usual meaning of Boltzmann constant, absolute temperature, and elementary charge, and a_{cis} and a_{trans} are the KCl solution activities in the cis and trans compartments, respectively.

VDAC voltage gating was measured using a previously described protocol (Colombini, 1989; Rostovtseva et al., 2006). A symmetrical 5-mHz triangular voltage wave of ±60 mV amplitude was applied with an Arbitrary Waveform Generator 33220A (Agilent). VDAC multichannel recordings were filtered by a low-pass 8-pole Bessel filter a 1 kHz, digitized at a sampling frequency of 2 Hz, and analyzed as described previously (Rostovtseva et al., 2006; Teijido et al., 2014) using pClamp v.10.7 software and an algorithm developed in-house (Rappaport et al., 2015). In each experiment, current records were collected from membranes containing >10 channels in response to enough periods of voltage waves to ensure a minimum of 100 channels per experiment. Only the part of the wave during which the channels were reopening was used for the subsequent analysis (Rappaport et al., 2015). Given the variable number of channels during each experiment, the average conductance (G) was normalized to the maximum conductance (G_{max}). The probability of the channel to be open, P_{open}, was defined as

$$P_{open} = \frac{G - G_{min}}{G_{max} - G_{min}}, \quad (2)$$

where G_{max} and G_{min} are the maximum and minimum conductances, corresponding to the channels mostly open at small voltages (<10 mV) and the channels mostly closed at high voltages (>50 mV), respectively. P_{open} plots were fitted according to the Boltzmann equation:

$$P_{open} = \left\{1 + \exp\left[\frac{F}{RT} \cdot n(|V| - V_0)\right]\right\}^{-1}, \quad (3)$$

where V_0 is the voltage at which half of the channels are open, n is the effective gating charge, and R, T, and F are the gas constant, absolute temperature, and Faraday constant, respectively.